

Geochemistry, Geophysics, Geosystems®



RESEARCH ARTICLE

10.1029/2021GC009753

Shallow-Water Tsunami Deposits: Evidence From Sediment Cores and Numerical Wave Propagation of the 1601 CE Lake Lucerne Event

Valentin Nigg¹ , Paola Bacigaluppi² , David F. Vetsch² , Hendrik Vogel¹ ,
Katrina Kremer^{1,3} , and Flavio S. Anselmetti¹ 

¹Institute of Geological Sciences, Oeschger Centre for Climate Change Research, University of Bern, Bern, Switzerland,

²Laboratory of Hydraulics, Hydrology and Glaciology, ETH Zürich, Zürich, Switzerland, ³Swiss Seismological Service, ETH Zürich, Zürich, Switzerland

Key Points:

- A siliciclastic-rich, normally graded sediment deposit is associated with the 1601 CE Lake Lucerne tsunami event
- Sedimentological analysis and radiocarbon dating were combined with numerical simulation to reconstruct the proposed depositional model
- Numerical simulation of the dimensionless bed shear-stress indicates the area of potential sediment source in the lagoonal environment

Supporting Information:

Supporting Information may be found in the online version of this article.

Correspondence to:

V. Nigg,
valentin.nigg@geo.unibe.ch

Citation:

Nigg, V., Bacigaluppi, P., Vetsch, D. F., Vogel, H., Kremer, K., & Anselmetti, F. S. (2021). Shallow-water tsunami deposits: Evidence from sediment cores and numerical wave propagation of the 1601 CE Lake Lucerne event. *Geochemistry, Geophysics, Geosystems*, 22, e2021GC009753. <https://doi.org/10.1029/2021GC009753>

Received 1 MAR 2021
Accepted 19 NOV 2021

Abstract The 1601 CE earthquake (M_w ca. 5.9) in “Unterwalden,” Central Switzerland, triggered multiple subaqueous mass movements and a subaerial rockfall that generated tsunami waves with run-up heights of up to 4 m and several hundred meters of inundation along the coastal lowlands of Lake Lucerne. In the shallow Lucerne Bay, historical chronicles reported an oscillation of the water with an initial amplitude of ~1–2 m and a period of 10 min, which continued for several days after the event with decreasing amplitude. Here, we investigate the lake-tsunami process chain from subaqueous mass movement-generated tsunami to wave propagation and ultimately to sediment resuspension, transport, and deposition in the shallow-water environment. The effects of the historical tsunami on Lucerne Bay are reconstructed using sediment-core analysis and numerical simulation of wave propagation. A 60-cm-thick event deposit was recovered along a sediment-core transect in the shallow waters and radiocarbon dated to 1306–1442 cal CE. The event deposit has a sharp basal contact with carbonate shell fragments followed upwards a normally graded succession of siliciclastic sand to silt with a high proportion of horizontally bedded wooden particles. The numerically simulated tsunami waves are characterized by a water-surface displacement of up to 1.5 m and generate bed shear-stresses that are likely capable of remobilizing large amounts of sediments in the Lucerne Bay area. Our study successfully links the sedimentology of event deposits with physical principles of sediment mobilization derived from numerical wave-forward modeling, providing a tool to improve the identification and interpretation of potential tsunami deposits.

Plain Language Summary An earthquake in Central Switzerland generated a tsunami on Lake Lucerne on 18 September 1601 CE, which is historically documented. The tsunami waves caused casualties, flooded coastal plains, and considerably damaged the lake shore. Previous studies have shown that several underwater landslides and a rockfall triggered by the earthquake generated the tsunami waves that propagated along the several lake basins. To better characterize this tsunami event, we examined sediment cores from the Lucerne Bay that host a sedimentary deposit, which has been associated to the historically reported event of 1601 CE. In addition, we numerically simulated the tsunami waves with specialized computer codes and studied the erosion potential in the Lucerne Bay.

1. Introduction

Tsunami hazard is frequently associated with megathrust earthquakes at convergent plate boundaries in the marine environment (e.g., 2011 Common Era [CE] Tohoku-Oki tsunami (Goto, Chagué-Goff, et al., 2011; Suzuki et al., 2011)). However, earthquake-triggered subaqueous mass movements have also generated devastating tsunamis that pose a threat to populated, low-lying coastal areas (e.g., 2018 CE Sulawesi earthquake (Heiderzadeh et al., 2019); 1998 CE Papua New Guinea Tsunami (Synolakis et al., 2002; Tappin et al., 1999)). In addition, subaerial landslides impacting on the water surface can generate devastating impulse waves with high initial run-up and destructive inundation (e.g., 1958 CE Lituya Bay landslide-generated impulse wave (Miller, 1961; Weiss et al., 2009); 2018 CE Anak Krakatau volcano collapse-generated impulse wave (Grilli et al., 2019; Paris et al., 2020; Putra et al., 2020)).

Where most tsunami evidence stems from the marine domain, tsunamis in lakes have recently been recognized as a considerable natural hazard with high magnitudes and low recurrence rates (Hilbe & Anselmetti, 2015;

© 2021 The Authors.

This is an open access article under the terms of the [Creative Commons Attribution-NonCommercial License](https://creativecommons.org/licenses/by-nc/4.0/), which permits use, distribution and reproduction in any medium, provided the original work is properly cited and is not used for commercial purposes.

Kremer et al., 2015, 2021; Nigg, Wohlwend, et al., 2021; Strupler, Danciu, et al., 2018; Strupler, Hilbe, et al., 2018). The most common mechanism that generate tsunamis in freshwater environments are large subaqueous and subaerial mass movements (Hilbe & Anselmetti, 2015; Kremer et al., 2021; Mountjoy et al., 2019; Nigg, Wohlwend, et al., 2021; Roberts et al., 2013; Strupler, Bacigaluppi, et al., 2020). Historic chronicles document that lacustrine tsunamis have caused fatalities, severe lake-shore erosion, and inundation in various lakes around the world (e.g., Lake Geneva, Switzerland [563 CE Tauredunum rockfall event (Favrod, 1991; Montandon, 1925)], Lake Lucerne, Switzerland (1601 CE Unterwalden earthquake (Cysat, 1969) and 1687 CE Muota Delta collapse (Bünti, 1973; Billeter, 1923; Dietrich, 1689)), Lake Baikal, Russia (1861 CE Tsagan earthquake (Klyuchevskii et al., 2012)). Prehistoric lake tsunamis were proposed based on subaqueous lake morphology in Lake Tahoe (Gardner et al., 2000; Moore et al., 2006), mass-movement event stratigraphy (Hilbe & Anselmetti, 2014; Kremer et al., 2015; Schnellmann et al., 2006; Siegenthaler et al., 1987), and numerical tsunami simulations (Hilbe & Anselmetti, 2015; Kremer et al., 2012; Mountjoy et al., 2019). To date, however, depositional signatures of tsunamis have received little attention in the freshwater environment. Roberts et al. (2013) document sedimentary signatures of the 2007 CE subaerial landslide-generated tsunami in the onshore setting of Lake Chehalis. Nigg, Wohlwend, et al. (2021) found sedimentary evidence of a prehistoric tsunami in the shallow-water and coastal area of Lake Sils, Switzerland, that are comparable to marine tsunami deposits.

Tsunami deposits are the accumulation of remobilized sediment from tsunami inundation and backwash in the on-, near- and offshore setting (Einsele et al., 1996) that provide information on the magnitude and recurrence of past events (Monecke et al., 2008). These deposits have been increasingly studied, especially in onshore areas, following the devastating 2004 CE Indian Ocean tsunami (Feldens et al., 2009; Paris et al., 2010; Sakuna et al., 2012; Sugawara et al., 2009) and 2011 CE Tohoku-Oki tsunami (Goto et al., 2014; Haraguchi et al., 2013; Ikehara et al., 2014; Tamura et al., 2015; Yoshikawa et al., 2015). In areas with discontinuous terrestrial records due to anthropogenic activity (Fritz et al., 2008; Goodman-Tchernov & Austin, 2015; Spiske et al., 2013), limited tsunami preservation (Spiske et al., 2013), and sediment-limited coastal settings (Apostsos et al., 2011), near-shore and offshore tsunami deposits may contribute to improved tsunami-hazard assessment in the future (Costa et al., 2021). Yet, the number of studies examining their signatures is rather small compared to their onshore counterparts (Costa & Andrade, 2020; Dawson & Stewart, 2008). This may be related to poor preservation of the primary deposits, especially due to reworking by wind-induced bottom currents above the storm-wave base (Weiss & Bahlburg, 2006) and by bioturbation from aquatic organisms (Van den Bergh et al., 2003). As tsunami backwash currents may transform into turbidity currents offshore (Einsele et al., 1996), the associated deposits are difficult or even impossible to distinguish from other turbidite deposits based on the textural appearance (e.g., seismo-turbidites, distal submarine slides, sediment plumes after heavy rainfall). Thus, proper contextualization and multidisciplinary approaches are needed for the identification and interpretation of offshore tsunami deposits (Costa et al., 2021).

In the nearshore environment, previous studies have successfully identified historic and prehistoric tsunami deposits (Abrantes et al., 2008; Goodman-Tchernov et al., 2009; Riou et al., 2020; Smedile et al., 2011; Van den Bergh et al., 2003). Their depositional signatures are characterized by a wide range of sedimentological characteristics (Fujiwara, 2008) including lower erosional surfaces (Ikehara et al., 2014; Riou et al., 2020; Smedile et al., 2020; Yoshikawa et al., 2015), coarse-grained clastic materials (Abrantes et al., 2008; Goodman-Tchernov et al., 2009; Paris et al., 2010; Sakuna et al., 2012; Van den Bergh et al., 2003), terrestrial-derived organics (Goodman-Tchernov et al., 2009; Paris et al., 2010; Sakuna et al., 2012), as well as single- and multiple-graded sandy deposits (Tamura et al., 2015). Though, no universal criteria for the recognition of shallow-water tsunami deposits exist since they depend on site specific conditions. Nevertheless, multiproxy-based sedimentological and geophysical methods combined with numerical simulation of sediment transport will help to improve the understanding of tsunami-induced sediment mobilization, transport, and deposition in the nearshore (Goto, Takahashi, et al., 2011; Noda et al., 2007).

Tsunami sediment-transport and deposition have increasingly been studied in onshore coastal environments using inverse (Huntington et al., 2007; Jaffe & Gelfenbaum, 2007; Jaffe et al., 2011, 2012; Johnson et al., 2017; Spiske et al., 2010; Tang & Weiss, 2015; Woodruff et al., 2008) and forward modeling (Apostsos et al., 2011, 2012; Ontowirjo et al., 2013; Pritchard & Dickinson, 2008). Inverse modeling uses the grain-size distribution of tsunami deposits to reconstruct tsunami flow-velocities (Jaffe & Gelfenbaum, 2007). Forward models, on the other hand, combine hydrodynamic and sediment-transport models (including erosion and deposition) to simulate observed

sedimentary deposits (e.g., grain-size and spatial-thickness distribution) (Aptosos et al., 2011). The successful combination of inverse and forward modeling in the 1755 CE Lisbon tsunami confirms the potential to improve understanding of historical events (Bosnic et al., 2021). Although, little attention has been drawn to the quantification of tsunami erosion in the nearshore area to date (Yoshikawa et al., 2015), Goto, Takahashi, et al. (2011) determined severely impaired stability of coastal infrastructures due to strong localized scouring and sediment rearrangement. Additionally, remarkable bathymetric changes caused by tsunamis were observed in several nearshore areas (e.g., Kirinda Harbor, Sri Lanka (Goto, Takahashi, et al., 2011)) and numerically simulated (Kuriyama et al., 2020), suggesting substantial sediment remobilization by tsunami waves in the shallow water.

Particle entrainment by flows has been quantified from empirical experiments (Mantz, 1977; Shields, 1936). It is strongly dependent on the bed shear-stress, flow regime, grain-size distribution, grain shape, grain packing, and density of the surface sediment (Boggs, 2014; Buffington & Montgomery, 1997). The resulting hydrodynamic description may be partially applied to tsunami-induced sediment transport in shallow water (Kihara et al., 2012). For the incipient motion of sediment particles by tsunami propagation, the fluid force, which consists of the bed-parallel drag force and the horizontal lift force, need to be larger than the resistance force of the particles to be moved (Lee & Balachandar, 2012; Van Rijn, 2007). For determining the threshold of sediment motion in uniform and non-uniform flows, the Shields diagram that relates the dimensionless bed shear-stress and the grain Reynolds number, can be used (Shields, 1936). Therefore, numerical simulation of the dimensionless bed shear-stress generated by tsunami propagation in the shallow-water environment can provide an indication of the sediment source location.

The main objective of this study is to find evidence for sediment remobilization in the Lucerne Bay caused by the 1601 CE Lake Lucerne tsunami using sediment cores, lake-bed samples, and numerical simulations of tsunami-wave propagation. First, we investigate the sedimentary structure and physical properties in the Lucerne Bay through a series of collected sediment cores and modern lake-bed samples. Then, we numerically simulate tsunami generation by one of the largest subaqueous mass movements triggered by the 1601 CE earthquake and examine the simulated wave characteristics (water-surface displacement, and flow-velocity magnitude) and spatial extent of threshold conditions for incipient motion using the dimensionless bed shear-stress (Shields parameter). This will ultimately help to provide a robust and sophisticated hypothesis on tsunami-induced sediment resuspension, transport, and deposition in the shallow-water setting of Lucerne Bay. The investigation of the lake-tsunami process chain will help to better understand tsunami hazard in lakes and sedimentary processes involved.

2. Study Site

Lake Lucerne is a perialpine lake located in Central Switzerland at an altitude of 433.6 m above sea level (asl). It lies geologically between the Helvetic nappes, the Subalpine Molasse, and the Swiss Molasse basin (Figure 1; Funk et al., 2013; Hantke et al., 2005; Kopp et al., 1955). The fjord-like lake consists of predominantly steep-sided lake shores and several subbasins with a maximum (max.) water depth of 214 m. The main tributary of Lake Lucerne is the Reuss River, which flows into the southeastern subbasin. There are several smaller tributaries in the subbasins. The outflow, Reuss River, is in the western part of the lake, in the Lucerne Bay.

Lucerne Bay is a relatively shallow subbasin with water depths between 2.5 to 5 m (max. water depth 8 m) and a sharp transition in the west leading to deeper parts of the lake (Figure 2). The basin is glacially eroded into Burdigalian sandstones of the Upper Marine Molasse and Aquitanian sandstones and conglomerates of the Lower Freshwater Molasse (Kopp et al., 1955; Schlunegger et al., 1997). The top of the bedrock occurs at a lowermost elevation of 408.8 m asl at the lake outlet (Keller, 2021) and at ~335 m asl at the Lucerne railway station in the southwest of the Lucerne Bay (Figure 2a, Keller, 2013) indicating strong contrasts in glacial overdeepening. The up to 100-m-thick overlying Quaternary deposits consist of a sedimentary succession formed by a thick package of Late Pleistocene sediments, characterized by glacially overconsolidated basal lodgment diamicts and local esker gravels above the bedrock surface, which are overlain by heterolithic glaciolacustrine silts with sand lenses (Keller, 2021). Around 14.7 kyr before present (BP), the area of the Lucerne Bay was filled with Late Pleistocene sediments up to 422 m asl at the Lucerne railway station and up to 426 m asl at the northern lake shore (Keller, 2021). These sediments are overlain by a relatively thin (1–4 m) sequence of transgressive-regressive Holocene deposits that comprise shallow-water to alluvial plain environments characterized as organic-rich swamp deposits, lacustrine carbonates, as well as deltaic deposits and gravelly lobes at the toe of incoming rivers

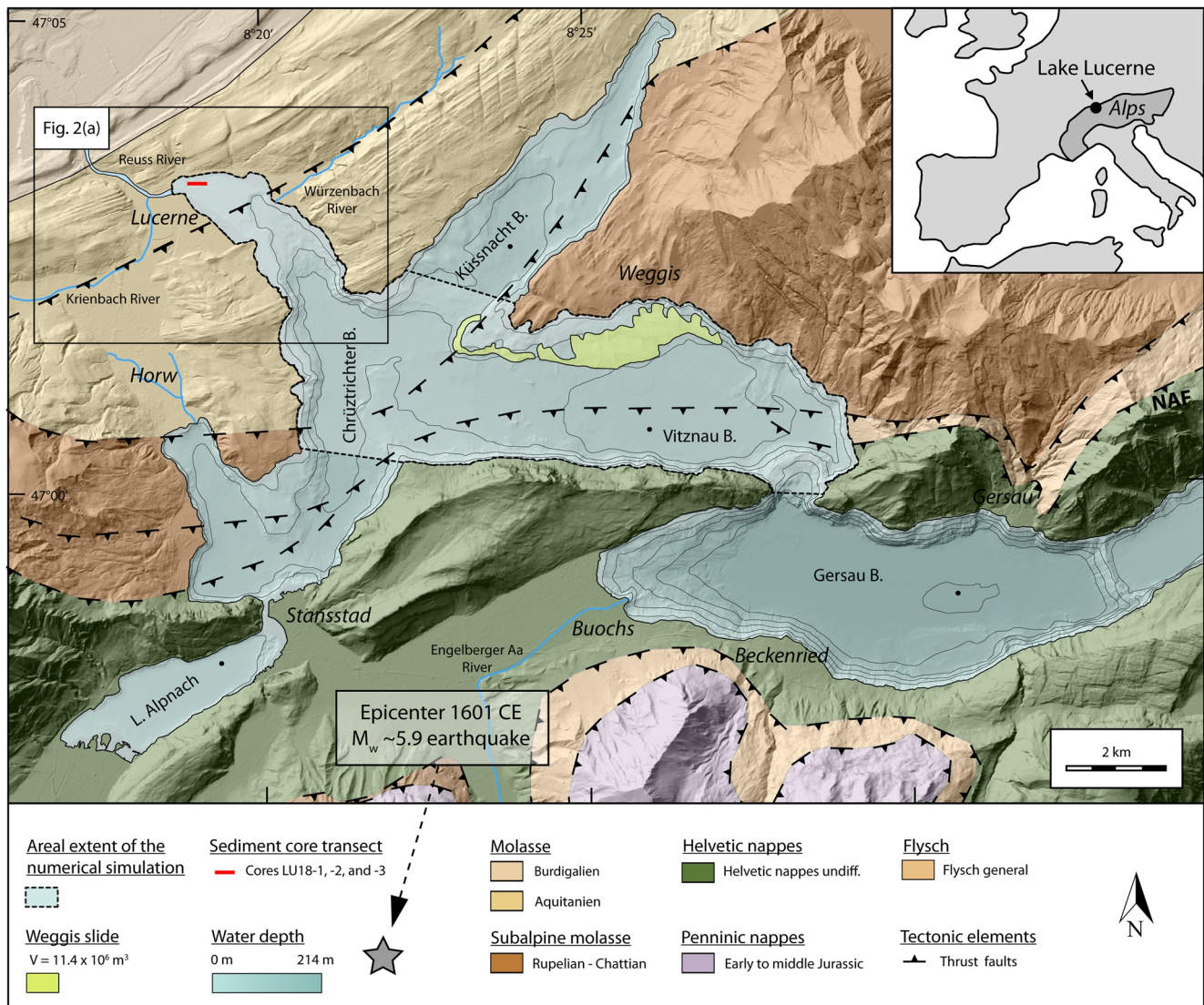


Figure 1. Western part of Lake Lucerne with individual lake basins (note that the Uri Basin in the east is not shown), giving the areal extent of the simulated Weggis slide (yellow), as well of the numerical simulation (light-blue area), the dashed line indicates open weir boundary condition toward adjacent lake basins. The map is based on the swisstopo swissALTI3D digital terrain model, geological map of swisstopo (GK500-Geol), and the bathymetry map of Hilbe et al. (2011).

(Keller, 2021). Major inflowing tributaries of the Lucerne Bay are the Würzenbach River in the northeast and the Kriensbach River in the southwest, delivering dominantly siliciclastic material (Figure 2a). The Würzenbach, entering the lake at the northern shore, is today artificially channelized, but formed a large delta over time. In the southern area of the City of Lucerne, the Kriensbach formed an extensive Holocene flood plain with gravelly alluvial fan deposits and overbank sands, which repeatedly clogged temporarily the lake outlet and caused high lake levels (Keller, 2013, 2021). Nowadays, the river is artificially diverted underground with tunnels feeding into the River Reuss (Figure 1).

Today, lake level is relatively stable at 433.6 m asl, with high lake levels in spring and late summer, and low lake levels in winter and peak summer (BAFU, 2009). Since the monitoring of the lake level in 1936 CE, the lowest lake level was measured in April 1938 CE at 433.15 m asl. The highest lake level was observed in September 2005 CE at 435.35 m asl (BAFU, 2009). At the time of the city foundation (~1200 CE) lake level was around 432.2–433.2 m asl (Keller, 2013). Through the construction of mills and a weir at the lake outlet in the thirteenth to fourteenth century, lake level was stabilized at 433.0 m asl (Keller, 2013). Prior to the historical record, lake level was presumably lower, with greater seasonal fluctuations (± 1.5 m; Keller, 2021). In the Late Glacial

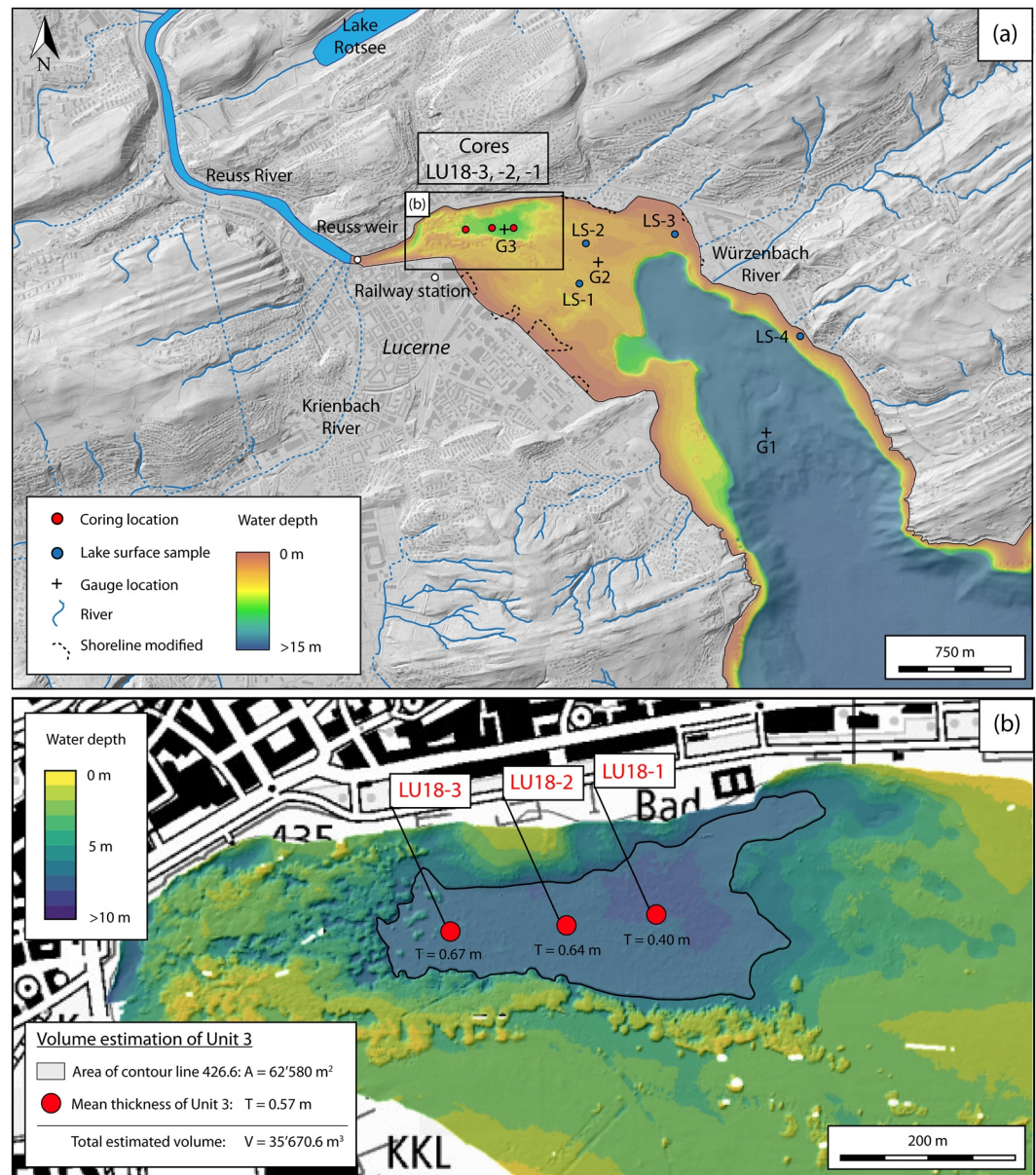


Figure 2. (a) Detailed map of the Lucerne Bay with the interpolated bathymetry (modified from Hilbe et al. (2011)) used for the numerical simulation with its outline (solid black line) and artificial obstacles such as landfills and coastal infrastructure that were cut off (today's shoreline course: dashed line). The map is based on the swisstopo digital terrain model swissALTI3D and the national map LK50 from swisstopo. The sediment core location (red dots), sediment core ID (red), surface sediment samples (blue dots), and virtual gauges (black crosses) plotted in Figure 11 are shown. (b) Detailed high-resolution bathymetric map (Hilbe et al., 2011) of the east-west oriented depression shows the sediment-core locations (red dots), thickness of the event deposit (Unit 3) observed in sediment cores, and the contour line 426.6 m asl (black outlined) used for the volume estimation of the siliciclastic-rich, normally graded Unit 3. The shallowest and rugged topography represents artifacts caused by aquatic plants.

Interstadial (~15–13 kyr BP), lake level was at ~432 m asl (Keller, 2021) and during the Neolithic Period (5–6 kyr BP) lake level was presumably lowest at around 428.6–429.5 m asl (Keller, 2013; Michel et al., 2012). After 1800 CE until today, strong artificial shoreline changes were carried out, especially around the City of Lucerne, but also around the lake in the vicinity of smaller villages.

2.1. The 1601 CE Earthquake and Lake Lucerne Tsunami

The earthquake on 18 September 1601 CE with an epicenter in “Unterwalden,” Central Switzerland (M_w ca. 5.9; Fäh et al., 2011; Schwarz-Zanetti et al., 2003) triggered multiple subaqueous mass movements in Lake Lucerne (Hilbe et al., 2011; Siegenthaler et al., 1987; Schnellmann et al., 2002, 2006) and a subaerial rockfall that impacted the lake surface simultaneously (Keller, 2017; Schnellmann et al., 2006; Schwarz-Zanetti et al., 2003). The two major subaqueous mass movements with estimated volumes of 11.4×10^6 and 20.8×10^6 m³ failed in the Vitznau and Gersau Basin, respectively (Hilbe & Anselmetti, 2015). Several smaller mass movements are observable from the lake bathymetry (Hilbe et al., 2011) and from seismic reflection data, and were attributed to this event (Schnellmann et al., 2006). These mass movements generated a basin-wide tsunami with wave heights exceeding 4 m on the northwestern shore of the Küssnacht Basin and devastating inundation and run-up along other parts of the lake shore (Cysat, 1969; Hilbe & Anselmetti, 2015). The alluvial plain near Buochs was inundated by about 750 m and mountains of water were documented from eyewitness reports in the Gersau Basin (Cysat, 1969). The event caused at least eight casualties, who were drowned by the tsunami waves in Beckenried (Cysat, 1969). However, no serious damage from the waves were reported in the City of Lucerne, although a lake-level oscillation (seiche) with an estimated amplitude of 1–2 m and a period of 10 min was reported (Cysat, 1969; Siegenthaler et al., 1987). The seiche caused a periodic drainage of the riverbed Reuss at the lake outlet (Cysat, 1969). With time, the amplitude decreased, but the seiche persisted for several days after the event (Cysat, 1969).

3. Methods

3.1. Site Survey and Sediment Sampling

High-resolution (1 m grid cell) bathymetric data of Lake Lucerne (Hilbe et al., 2011) were used for the coring-site selection (Figure 2b). Seismic reflection data were acquired using a 3.5 kHz pinger system along the sediment-core transect. Three sediment cores (Core LU18-1, -2, and -3) were recovered from a floating platform in water depths between 7 to 8 m (Figure 2b) with a 3-m-long percussion piston-coring system (UWITEC Co. Austria) up to a subsurface depth of 3.5 m. A gravity corer was used to recover the undisturbed water-sediment interface. Lake-bed sediment samples were collected at four locations along the Lucerne Bay (Figure 2a).

3.1.1. Sediment Cores

Petrophysical properties (gamma ray attenuation bulk density, magnetic susceptibility, and p-wave velocity) were measured on all recovered whole round cores with a Geotek multi-sensor core logger (MSCL-S). Whole-round cores also underwent X-ray computed tomography (CT) imaging using a medical Siemens Somatom Definition AS scanner. Full core CT-scan data were obtained at a voxel size of 100 μ m and visualized with the RadiAnt DICOM Viewer software (version 4.6.9.18463). Sediment cores were split longitudinally, imaged with the MSCL-S core logger line-scan camera, and sedimentologically described. A complete composite sediment record was obtained by visual correlation of overlapping piston and gravity cores. High-resolution assessment of sediment geochemistry by means of X-ray fluorescence (XRF) scanning was performed on split core surfaces of Core LU18-2 with an ITRAX-XRF core scanner (Cox Ltd., Sweden). Measurements were performed with a Cr-tube set to 30 kV and 50 mA using longitudinal 2 mm integrals and 20 s integration times. Here, we report relative intensities of calcium (Ca) and silicon (Si) to titanium (Ti) and aluminum (Al), respectively.

Sediment samples were continuously taken at 10 cm intervals in Units 4 and 3 (Core LU18-2) and at 1 cm intervals in Unit 2 (Core LU18-1) for elemental analysis of carbon, nitrogen, and sulfur (CNS). Only two subsamples were taken from the top of Unit 1 (Core LU18-1) due to its presumably glaciolacustrine sediment appearance. All sediment subsamples were freeze-dried and homogenized using mortar and pestle. Total carbon (TC), total nitrogen (TN), and total sulfur (TS) concentrations were measured on these samples with a Flash 2000 NCS (Thermo Fisher Scientific Co.) combustion elemental analyzer configured with a MAS plus autosampler (Thermo Fisher Scientific Co.) and thermal conductivity detector. Samples were weighed into tin (5–8 mg) capsules for TC, TN, and TS measurements and silver (4–5 mg) capsules for total organic carbon (TOC) measurements. For TOC concentration measurements samples were treated with 1M HCl until no visual reaction occurred. The remaining HCl was evaporated prior to flash combustion analysis. Total inorganic carbon (TIC) was calculated from the differences between TC and TOC. The molar carbon-to-nitrogen (C/N) ratio was determined from TOC and TN concentrations. CaCO₃ was calculated from TIC using the stoichiometric conversion factor of 8.33.

For grain-size analysis of a sandy deposit (Unit 3), sediment samples were taken continuously at 1 cm intervals between 37 and 120 cm depth in Core LU18-2. Subsamples with a wet weight of ~1 g were treated with 10 volume percentage (vol%) HCl and 10 vol% H₂O₂ to remove solid carbonate species and organic matter. A dispersion solution containing Na₆P₆O₁₈ and Na₂CO₃ was added to the remaining clastic fraction and shaken in aqueous suspension for an 1 hr prior to analysis. Laser diffraction analysis (LDA) was then carried out with a Malvern Mastersizer 3000 particle size analyzer. Grain-size distribution was calculated for each sample from the average of three aliquot measurements. Grain-size classes are presented after the classification proposed by Wentworth (1922).

Radiocarbon dating of terrestrial plant macro-remains from Core LU18-2 was applied to date a sandy deposit (Unit 3). A sample was taken both directly below and above Unit 3. Four samples were taken at regular intervals from the sandy deposit (Unit 3). Samples were measured by accelerator mass spectrometry (AMS) with the Mini RadioCarbon Dating System at the Department of Chemistry and Biochemistry, University of Bern. Radiocarbon ages were calibrated into calendar years Common Era (cal CE) using the OxCal software (version 4.3; Ramsey, 2009) and the IntCal20 Northern Hemisphere calibration curve (Reimer et al., 2020). Radiocarbon measurements of post-bomb samples are reported in fraction modern ¹⁴C (F¹⁴C; Reimer et al., 2004).

3.1.2. Lake-Bed Sediment

Lake-bed sediment samples (uppermost ~10 cm) were collected at four locations (LS-1 to LS-4) in Lucerne Bay by diving with a shovel and a bucket during summer from a sailboat (Figure 2a). The collected samples were described macroscopically using a binocular. TC, TN, TS, and TOC concentrations were measured, and TIC and CaCO₃ concentrations as well as the molar C/N ratio was calculated according to the procedure described above. For the grain-size analysis of the lake-bed sediment samples the same procedure as explained in the previous section was performed.

3.1.3. Estimation of Sediment Volume of Unit 3

The depositional volume of Unit 3 was estimated based on the high-resolution bathymetric data from Hilbe et al. (2011) and the thickness of Unit 3 observed in sediment cores. Because of the low vertical penetration of the seismic reflection data, probably due to the strong absorption of the acoustic signal in the uppermost gas-rich sediment in the Lucerne Bay, the data could not be used to characterize the spatial distribution of the sedimentary units. Therefore, the depositional volume was estimated based on the 426.6 m asl contour line, as this delimits the depression edge. The area was calculated using ArcMap (version 10.8). The estimated depositional volume of Unit 3 was calculated based on the mean thickness of the unit observed in the sediment cores and the mapped polygon of the 426.6 m asl contour line.

3.2. Numerical Simulation, Validation, Visualization, and Sensitivity Analysis of the Bed Shear-Stress

The wave generation, propagation, and inundation were numerically simulated with the freeware BASEMENT (BAsic-Simulation-EnvironMENT; www.basement.ethz.ch). The software is originally designed for quasi-1D and 2D simulations of river hydro- and morpho-dynamics in alpine and subalpine regions. It enables the simulation of steady and unsteady hydraulic flow conditions with complex geometries as well as sediment transport. For the present study, the underlying mathematical description is based on a decoupled system of equations given by the 2D-depth averaged non-linear shallow-water model for hydrodynamics and the Exner equation for morphodynamics (Vanzo et al., 2021). BASEMENT is based on the shallow-water equations and is thus very similar to common tsunami codes such as GeoClaw (Berger et al., 2011). Finite volume spatial discretization in combination with Riemann solver guarantees the stability and robustness of the numerical solution (Vetsch et al., 2020). Due to its highly optimized design, the software allows for accelerated simulations using multi-core central processing units (CPUs), graphic processing units (GPUs), and hybrid CPU/GPU-systems.

For hydrodynamic simulations, BASEMENT computes the water-surface elevation h and the specific water-discharge in horizontal x - and y -direction, q_x and q_y , respectively, in a selected computational domain. From these quantities, the water-surface displacement

$$A = h - h_{\text{ref}},$$

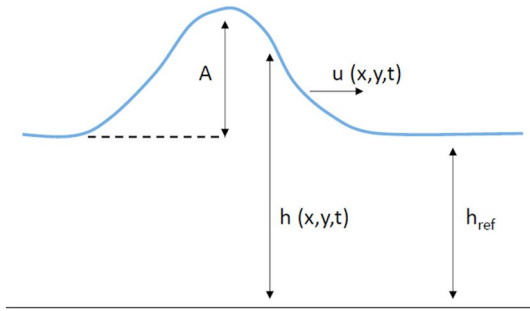


Figure 3. Sketch of computed numerical quantities: initial still-water reference level (h_{ref}), water-surface elevation (h), water-surface displacement (A), and flow-velocity magnitude (u).

with h_{ref} defined as the initial still-water reference-level and the flow-velocity magnitude,

$$u = \frac{\sqrt{q_x^2 + q_y^2}}{h}$$

can be derived (Figure 3). The bed shear-stress is defined as,

$$\tau = \frac{u^2 \rho_f}{c_f^2},$$

with ρ_f fluid density, c_f friction coefficient for fully turbulent flow computed according to Chézy as,

$$c_f = 5.75 \log\left(12 \frac{h}{k_b}\right)$$

(Bobrowsky & Marker, 2018) and bed roughness (k_b), which may range from grain roughness to total physical bed-roughness as mentioned in Houwman and Van Rijn (1999). The dimensionless bed shear-stress derived by Shields (1936) based on dimensional analysis (also known as the Shields parameter) is defined as,

$$\theta = \frac{\tau}{(\rho_s - \rho_f)gd_s},$$

where ρ_s represents the sediment density, g the gravitational acceleration, and d_s the grain diameter of bed-surface sediment.

The considered computational domain is limited to the Vitznau Basin and the Lucerne Bay with open boundaries (non-reflective boundary condition) to allow a natural outflow toward the Gersau, Küssnacht, and Horw Basins and at the lake outlet in the Lucerne Bay (Figure 1). To account for inundation and backwash in the Lucerne Bay, the computational domain includes the first 100–200 m onshore, depending on the topography. The digital elevation model is based on the high-resolution bathymetric data obtained by Hilbe et al. (2011), which was resampled to a cell size of 25 m². Shallow-water areas (water depth 0–4 m), which are not entirely covered by the bathymetric data were linearly interpolated to the current shoreline with ArcMap (version 10.8.1), whereas large artificial obstacles (islands and port facilities) were cut out (Figure 2). From the resampled bathymetry, the computational grid with 787.4k triangular elements with an average cell size of 115 m² in the central Vitznau Basin and 25 m² in the Lucerne Bay area was created.

The numerical simulation of the 1601 CE Lake Lucerne tsunami is based on the bathymetric reconstruction of the Vitznau Basin prior to the earthquake by Hilbe and Anselmetti (2015) (Figure 1). The Weggis slide with an area of 2.3 km² and a total failed volume of 11.4×10^6 m³ was simulated by an instantaneous downward vertical displacement of the water column along the area by 5 m. This corresponds to the total failed masses of the Weggis slide during the 1601 CE event. Total simulation time for the wave propagation is set at 1,800 s after the instantaneous collapse. The BASEMENT simulation was computed within 312 s on a NVIDIA Tesla P100 PCIe-12GB GPU card.

For the validation of the tsunami propagation computed with BASEMENT, obtained results were compared with the numerical simulation of Hilbe and Anselmetti (2015) considering the complete lake. Hilbe and Anselmetti (2015) used MassMov2D for the mass-movement using a Bingham plastic material and GeoClaw for the wave propagation simulation. Their results agree well with the historical description of the tsunami. Both BASEMENT and GeoClaw are based on the same hydrodynamic approach for the numerical wave propagation simulation. However, the tsunami triggering mechanism used in our study is strongly simplified compared to the simulation performed by Hilbe and Anselmetti (2015). To validate the use of an instantaneous collapse of the Weggis slide for the wave generation, we compared the max. water-surface elevation on the lake and the max. flow depth onshore.

The dimensionless bed shear-stress was simulated using conservative values of the physical bed roughness (k_b) from 0.0002 to 0.1 m. According to Houwman and Van Rijn (1999), this is a reasonable range from grain

roughness to the total bed roughness. The computed dimensionless bed shear-stress was used particularly as an indicator for the area of potential sediment sources in the Lucerne Bay.

Data visualization was performed with the numerical data visualization software Paraview (V5.8.1, www.paraview.org). Three virtual gauges were placed in the Lucerne Bay. Gauge 1 is located at the entrance of the Lucerne Bay, gauge 2 in the shallow-water area, and gauge 3 in the east-west oriented depression, where sediment cores were retrieved (Figure 2a). Time series of water-surface displacement, flow-velocity magnitude, specific discharge, bed shear-stress, and dimensionless bed shear-stress (Shields parameter) were investigated using gauge data (Figures S1, S2, and S3 in Supporting Information S1). In addition, the spatial variability of the variables at different time steps was analyzed on map scale. The area with a dimensionless bed shear-stress $\theta \geq 0.03$ in Lucerne Bay was calculated with ArcMap (version 10.8.1). Flow field vectors were used to reconstruct the flow path and direction of potential sediment transport.

4. Results

4.1. Sediment-Core Data

Based on the high-resolution bathymetric data (Hilbe et al., 2011) a topographic depression was identified in the Lucerne Bay near the lake outlet (Figure 2b). The depressional feature is characterized by an east-west oriented longitudinal shape with a length of ~ 400 m, a width of ~ 200 m, and an average water depth of 7.5 m. The surrounding plateau of the Lucerne Bay has a water depth of ~ 3.5 m. This depression surrounded by shallow water provides an ideal depositional environment suitable for trapping remobilized sediment from tsunami propagation, inundation, and backwash in the Lucerne Bay. Three sediment cores (LU18-1, LU18-2, and LU18-3) were retrieved along an east-west oriented transect within the depression (Figure 2; see Table S1 in Supporting Information S1 for coordinates of core location).

Recovered sediment cores have a complete composite sediment record of 284 cm (Core LU18-1), 288 cm (Core LU18-2), and 218 cm (Core LU18-3). The lithostratigraphy consist of four well-traceable sedimentary units (Figure 4) observed along the sediment-core transect (Figure 5), which were identified by visual appearance and core-log data (Figure 6). See Table S2 in Supporting Information S1 for results of the CNS measurements in Unit 1, 2, 3, and 4.

4.1.1. Sedimentary Unit Description

4.1.1.1. Unit 1: Dense—Cohesive Silty Clay

Unit 1 is light gray in color and consists of a cohesive, very dense (~ 2.1 g cm $^{-3}$), silty, clay-rich sedimentary deposit with up to cm-thick graded sandy layers. The fine laminae with variable thickness and graded fine sand to silt are well recognizable on the CT-grayscale images (Figure 6). These graded intervals are also well expressed in the XRF Si/Al ratio that may be used as grain-size indicator (Figure 6). Magnetic susceptibility varies only slightly within the unit ($7\text{--}12 \times 10^{-5}$ SI). Elemental analyses were only conducted in the uppermost centimeter of the unit because of its glaciolacustrine appearance. Analysis yields low TOC (0.2–0.5 wt%), TN (0.0–0.4 wt%), and TS (0.0–0.03 wt%). CaCO $_3$ amounts up to 37 wt% (Figure 7).

4.1.1.2. Unit 2: Light Brown Gyttja

Unit 2 is a light brown gyttja with occasional beige laminae, variable thickness between 2 and 10 cm with coarse sand and carbonate shell fragments embedded in an organic-rich matrix with low density (1.7 g cm $^{-3}$), and a transitional base over >2 cm (Subunit 2 $_T$) (Figures 4, 5, and 7). The transitional base of Unit 2 is brownish gray in color and consists of fine to medium sand with carbonate shell fragments and a distinct peak in the XRF Ca/Ti ratio (Figure 6). Along the sediment-core transect the transitional base has variable thickness in the cm-range. Finely embedded coarse sand and carbonate shell fragments are well recognizable in the low density, organic-matter-rich matrix with CT-grayscale image (Figure 7). TOC is low at the lower transitional base (~ 0.4 wt%) and increases gradually to 1.5–2 wt% in the upper part (91–83 cm) of the unit. The C/N ratio varies between 9.5 to 13 mol mol $^{-1}$ and sulfur is between 0.0 and 0.2 wt% (Figure 7). CaCO $_3$ varies between 13 and 54 wt% and is highest within the beige laminae (Figure 7). Magnetic susceptibility is $\sim 3 \times 10^{-5}$ SI (Figure 6).

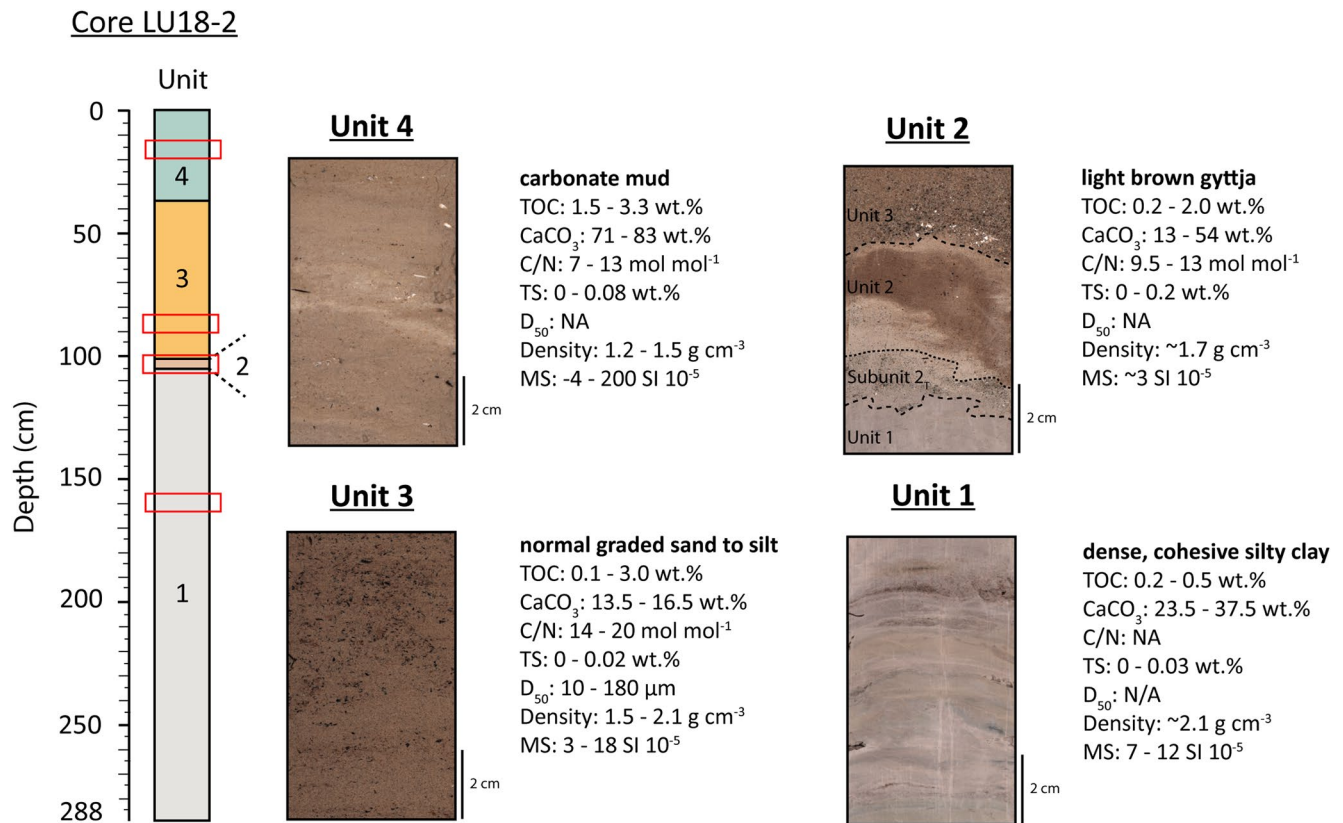


Figure 4. Complete composite sediment Core LU18-2, selected line-scan images of the four lithologic units, and its sedimentologic properties (TOC, CaCO₃, and TS concentrations, as well as molar C/N ratio, D₅₀ of the laser diffraction analysis grain-size distribution, density, and magnetic susceptibility). Red boxes show the location of the line-scan images in the sediment-core log. Note that in the line-scan image of Unit 2, the lower transitional base (Subunit 2_r) to Unit 1 and the upper sharp contact to Unit 3 are indicated with a dashed black line.

4.1.1.3. Unit 3: Normally Graded Sand to Silt

Unit 3 is dark brown in color and consists of a thick (40–67 cm), dense, siliciclastic, normally graded fine to medium sand with sharp lower and upper contacts (Figures 6 and 8). Coarse sand-sized shell fragments are finely dispersed in a fine siliciclastic sand at the bottom of the unit. The enrichment of macroscopically observed carbonate shell fragments at the bottom is also expressed in the distinct peak in the XRF Ca/Ti ratio at the base (Figure 6). In the upper part, carbonate is homogeneously present (13.5–16.5 wt%) and is occasionally found as fine sand-sized shell fragments. The C/N ratio (14–20 mol mol⁻¹) could only be calculated in the top three subsamples at 60, 50, and 40 cm core depth, but not in the lower subsamples due to nitrogen concentrations below detection limit (Figure 6). The high C/N ratio fits well with the observation of a significant amount of macroscopic, horizontally embedded wood fragments, whose abundance increases toward the top of the unit. Magnetic susceptibility ranges from 3 to 18 × 10⁻⁵ SI, and density decreases upcore from 2.1 to 1.5 g cm⁻³ (Figure 6). Similarly, the mean grain size (D₅₀) and sorting decreases upcore from well sorted fine sand (D₅₀: 90–180 μm) at the base to moderately sorted silt between 55–60 cm core depth and poorly sorted silt at the top (Figure 8). The XRF Si/Al ratio correlates well with the LDA grain-size data and can be used as grain-size indicator (Figure 6).

4.1.1.4. Unit 4: Lacustrine Carbonate

Unit 4 is light gray in color, varies in thickness between 17 and 43 cm along the sediment-core transect (Figure 5), and consists of shell fragments embedded in an endogenous carbonate clayey silt-sized matrix, with siliciclastic minerals only as accessories. It has a CaCO₃ concentration of 70–80 wt%, a gradual increase in TOC (1.5–3.3 wt%) upcore, and a decrease in the C/N ratio (13–7 mol mol⁻¹) and density (1.5–1.2 g cm⁻³) (Figure 6). Magnetic susceptibility has a peak at 27.5 cm depth (197.5 × 10⁻⁵ SI), which correlates with the occurrence of metalliclly shiny, black, gravel-sized coal particles. In the upper 20 cm, the magnetic susceptibility is slightly negative

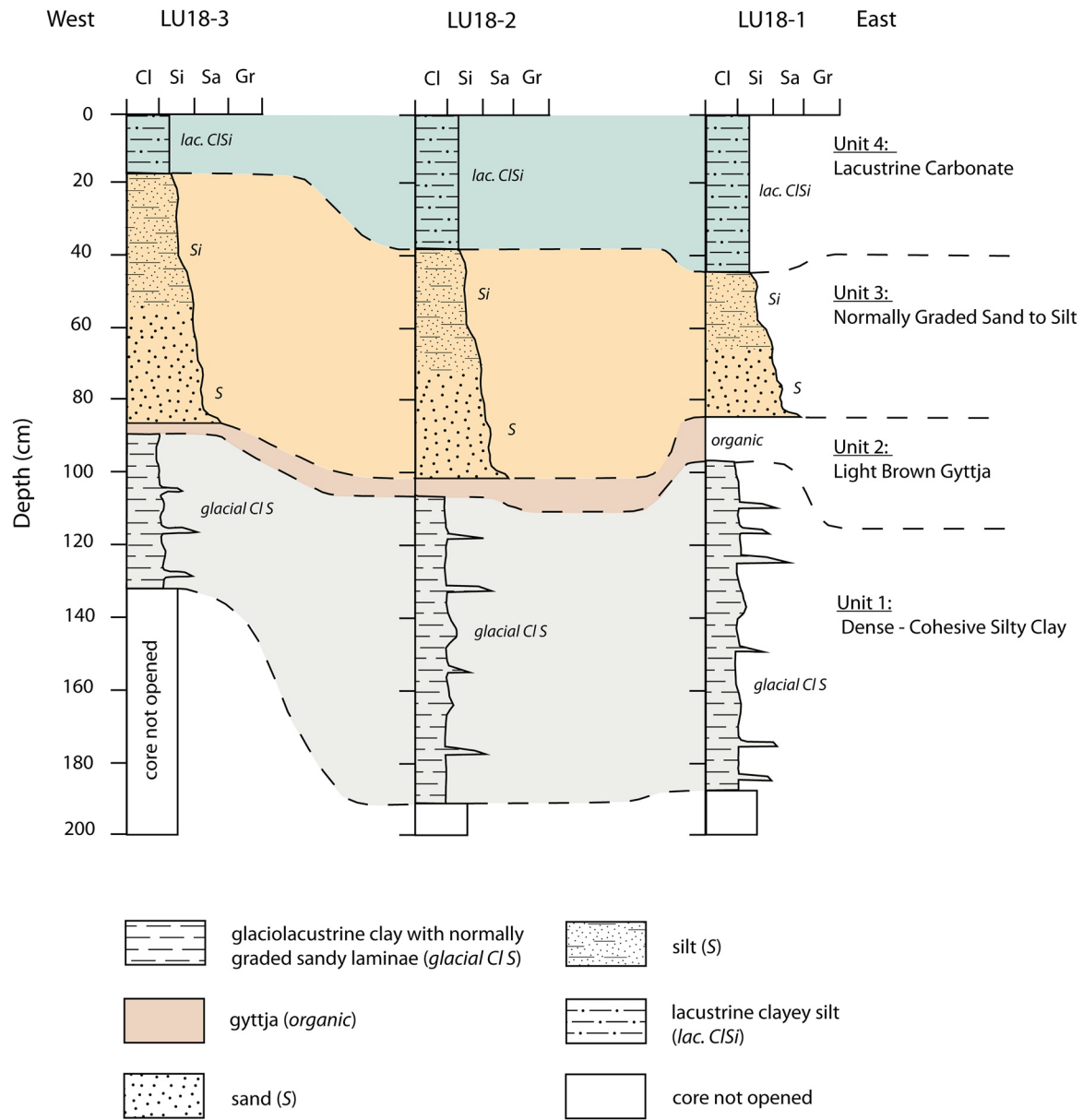


Figure 5. Lithological profile of the sediment-core transect (Cores LU18-1, LU18-2, and LU18-3) recovered along the east-west oriented depression in the Lucerne Bay, Lake Lucerne (Figure 2b).

(-4×10^{-5} SI). The XRF Ca/Ti ratio is very irregular in the lower part of Unit 4 (Figure 6). This is likely related to the metallic shiny gravel-sized coal particles causing an undulous sediment surface in this core section.

4.2. Radiocarbon Dating

A total of six radiocarbon dates were obtained from terrestrial organic macro-remains (Table 1). Four samples that were collected at regular intervals in Unit 3 have calibrated radiocarbon ages in the range of 1306–1442 cal CE (Table 1, Figure 6). One sample of fragmented leaves from Unit 2 yields a radiocarbon age of 1174–1277 cal CE. Another sample of leaf fragments from the lowermost section of Unit 4 has a modern radiocarbon age (Table 1). The calibrated radiocarbon age ranges are given within a 2σ confidence level, which corresponds to a 95.4% probability.

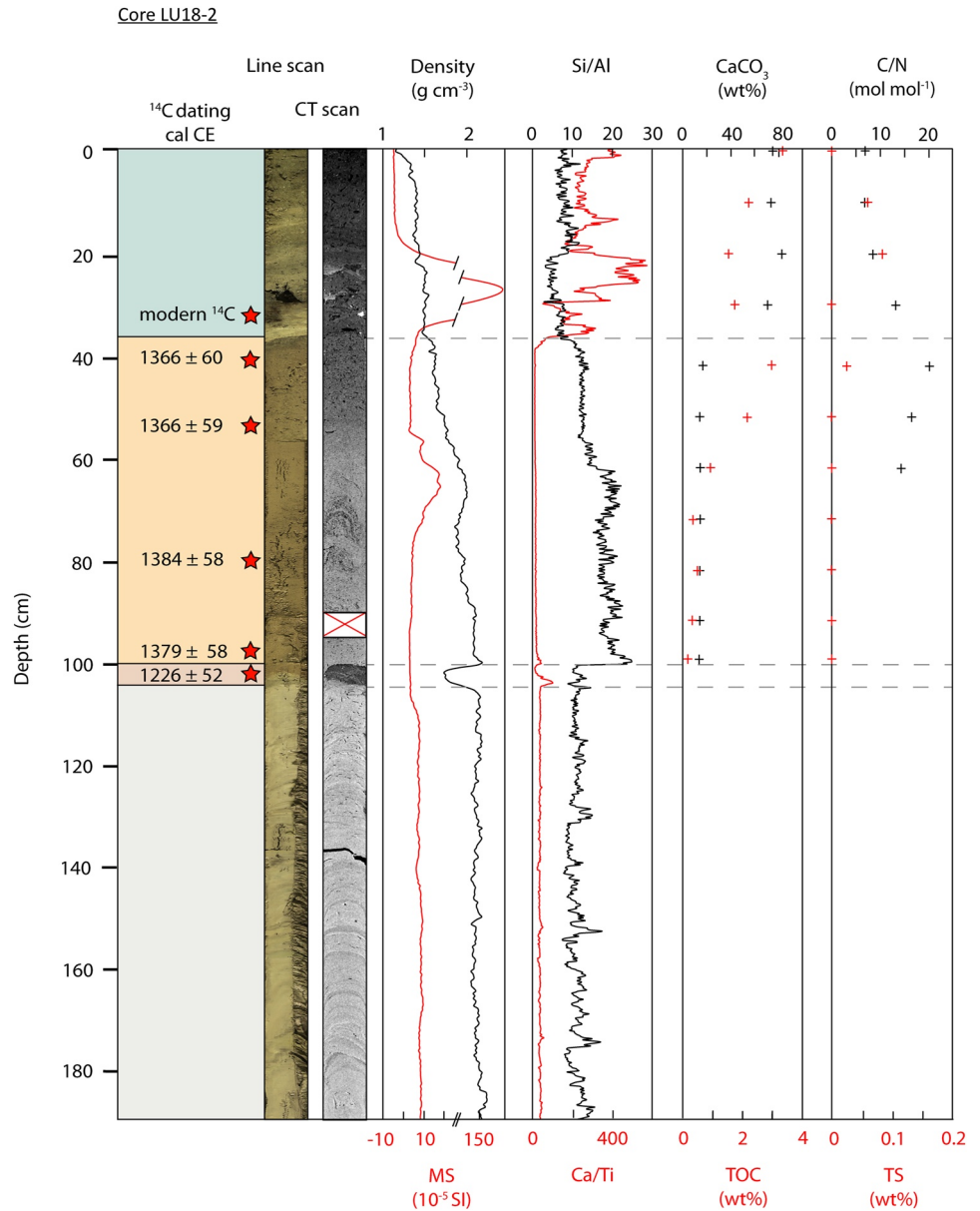


Figure 6. Sediment Core LU18-2 shows calibrated radiocarbon ages, line-scan image, CT-grayscale image, density, magnetic susceptibility, Si/Al and Ca/Ti ratio from the XRF scans, CaCO₃, TOC and TS concentrations, and molar C/N ratio. See Figure 7 for results of Unit 1 and 2 analyzed in Core LU18-1.

4.3. Volume Estimation of Unit 3

The estimation of the total volume of Unit 3 along the east-west oriented depression is based on high-resolution bathymetry data and retrieved sediment cores. The polygon of contour line 426.6 m asl has an area of 62'580 m² (Figure 2b). The thickness of Unit 3 is 0.4 m in Core LU18-1, 0.64 m in Core LU18-2, and 0.67 m in Core LU18-3, respectively. The mean thickness is 0.57 m, corresponding to a total estimated depositional volume of 35'670.6 m³ (Figure 2b; Table S3 in Supporting Information S1).

4.4. Lake-Bed Sediments

Four lake-bed sediment samples (LS-1 to LS-4) were collected in the Lucerne Bay (Figure 2a). Sample LS-1 and LS-2 were collected in the central part of the Lucerne Bay. Sample LS-3 is taken in the western part of the

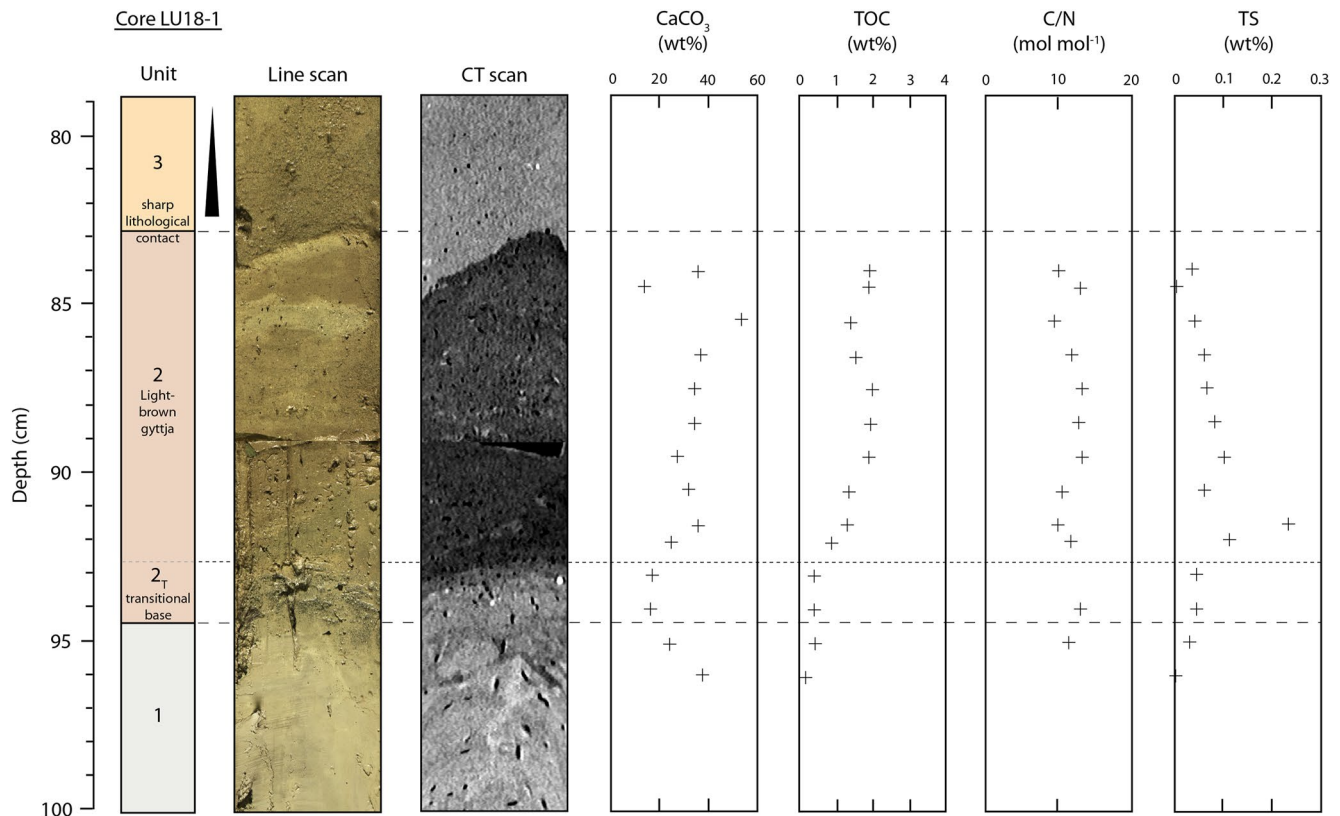


Figure 7. Line-scan image, CT-grayscale image, CaCO₃, TOC and TS concentrations, and the molar C/N ratio of subsamples from Unit 2, its lower transitional base (Unit 2_T) and the uppermost of Unit 1 in Core LU18-1. The sharp basal contact of Unit 3 is well recognizable in the CT-grayscale image.

Würzenbach River delta, and Sample LS-4 on the northeastern lake shore of the Lucerne Bay. See Table S4 in Supporting Information S1 for coordinates of the sample location. The four lake-bed sediment samples (Table 2) are characterized as lacustrine marl with sand-sized carbonate shell fragments, and coarse organic remains (Sample LS-1 and LS-2), poorly sorted siliciclastic sand with fine gravel and carbonate shells (Sample LS-3), and a mixture of siliciclastic fines and lacustrine carbonate fine sandy silt with coarse organic remains (Sample LS-4). See Table S5 in Supporting Information S1 for the results of the elemental analyses of CNS.

4.5. Numerical Tsunami Simulation

4.5.1. Validation of the Numerical Simulation

For the validation of the numerical simulation, results were qualitatively and quantitatively compared with the numerical simulation of Hilbe and Anselmetti (2015) (Figure 9). The max. water-surface displacement of both numerical simulations shows very good agreement in the Vitznau Basin and good agreement in the Lucerne Bay area (Figure 9a). For example, on the southeast coast Lucerne Bay the two simulation have nearly identical results. However, the southwest coast shows higher values for BASEMENT. Proximal to the tsunami source at Weggis, max. flow depth, and inundation distance agree well, but also here the BASEMENT simulation shows locally higher values of up to 1 m (Figure 9b). The discrepancy could be addressed to the evaluation of max. water-surface displacement and flow depth, because Hilbe and Anselmetti (2015) did not provide precise information about this. The numbers may indicate an average value over a certain area or, as in the case of BASEMENT, the local maximum value.

4.5.2. Tsunami Generation and Propagation

The 1601 CE Weggis-slide collapse with a volume of $11.4 \times 10^6 \text{ m}^3$ (Hilbe & Anselmetti, 2015) was simulated by an instantaneous collapse of a 5 m thick sediment drape located on the northern lateral slope of the Vitznau Basin (Figure 1). This moving slab and the affected area ($>2 \text{ km}^2$) correspond to the well-defined 1601 CE Weggis slide

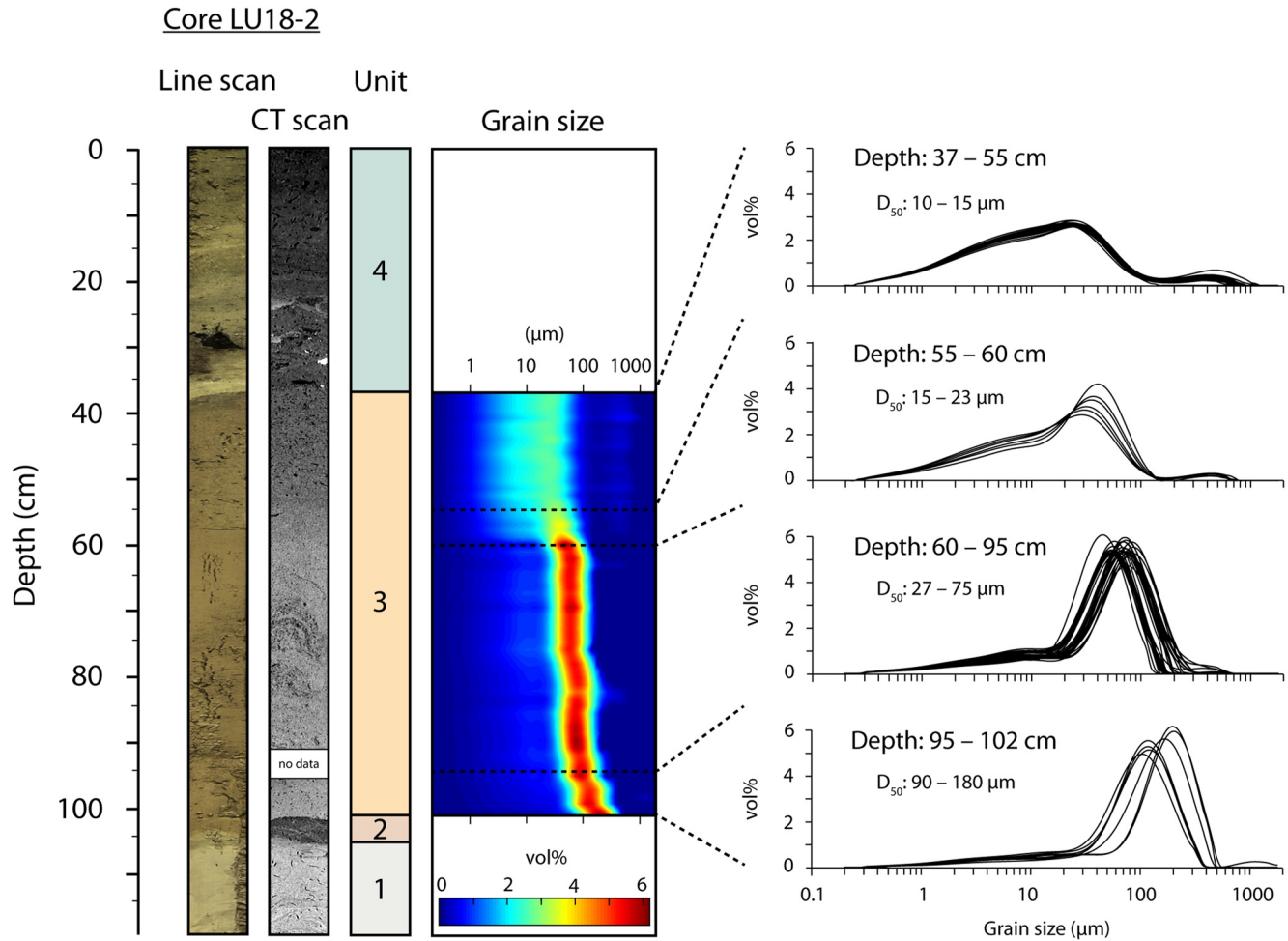


Figure 8. Line-scan image, CT-grayscale image, and particle-size distribution from the laser diffraction analysis of Unit 3 in Core LU18-2. The grain-size distribution of the siliciclastic fraction shows a pronounced fining upward trend.

described by Schnellmann et al. (2005) and Hilbe and Anselmetti (2015). The numerically simulated wave generation and propagation can be divided in three phases: wave generation (phase 1), wave propagation in the Vitznau Basin (phase 2), and arrival of a first wave trough in the Lucerne Bay that is followed by three main wave pulses (phase 3). See Movie S1 in Supporting Information S1 for the animation of the wave propagation simulation.

Table 1
AMS Radiocarbon Age and $\delta^{13}\text{C}$ Results From Terrestrial Organic Macro-Remains From Core LU18-2

Sample	Core depth (cm)	Lithological unit	Sample material	$\delta^{13}\text{C}$ (‰)	^{14}C age $\pm 1\sigma$ (^{14}C years BP) ^a	Calibrated 2σ -range (cal CE) ^{b, c}
BE-10751.1.1	35–36	4	Leaf fragments	−28.7	<0 ^d	Modern
BE-10752.1.1	41–42	3	Conifer needle	−28.7	570 \pm 31	1306–1425
BE-10753.1.1	54–55	3	Conifer needle	−28.8	567 \pm 30	1307–1425
BE-10754.1.1	79–80	3	Conifer needle	−27.4	527 \pm 31	1326–1442
BE-10755.1.1	98–99	3	Leaf fragments	−31.8	544 \pm 30	1321–1437
BE-10756.1.1	102–103	2	Leaf fragments	−29.7	812 \pm 36	1174–1277

Note. Radiocarbon age uncertainties refer to 1-sigma uncertainties. Range of calibrated represent 95.4% probability (2σ). AMS, accelerator mass spectrometry.

^aStuiver and Polach (1977). ^bRamsey (2009). ^cReimer et al. (2020). ^dF¹⁴C = 1.0738 \pm 0.0041.

Table 2

Lake-Bed Sediment Samples Collected in the Shallow Area of the Lucerne Bay: Sample ID, Macroscopic Description, TOC and CaCO₃ Concentrations, Molar C/N Ratio, D₅₀ of the Grain-Size Distribution as Well as the Volume Percentage of the Clay-, Silt-, and Sand Fraction

Sample ID	Macroscopic description	TOC (wt%)	CaCO ₃ (wt%)	C/N ratio (mol mol ⁻¹)	D ₅₀ (μm)	Clay (vol%)	Silt (vol%)	Sand (vol%)
LS-1	Lacustrine marl with sand-sized carbonate shell fragments and coarse organic material	2.208	80.8	6.7	45	3	60	37
LS-2	Lacustrine marl with sand-sized carbonate shell fragments and coarse organic material	2.424	78.4	6.8	58	3	50	47
LS-3	Poorly sorted siliciclastic sand with fine gravel	0.427	5.1	7.5	340	0	3	97
LS-4	Mixture of siliciclastic fines and lacustrine carbonate fine sandy silt with coarse organic material	2.481	26.9	9	45	3	62	35

A wave trough with a water-surface displacement with respect to the lake at rest of more than -3 m forms immediately after the instantaneous subaqueous collapse along the failed area (Figure 10a). In the initial phase, a wave trough approaches the proximal shore after 20 s (Figure 10b). After 40 s wave crests of 2 m reach the nearest shore

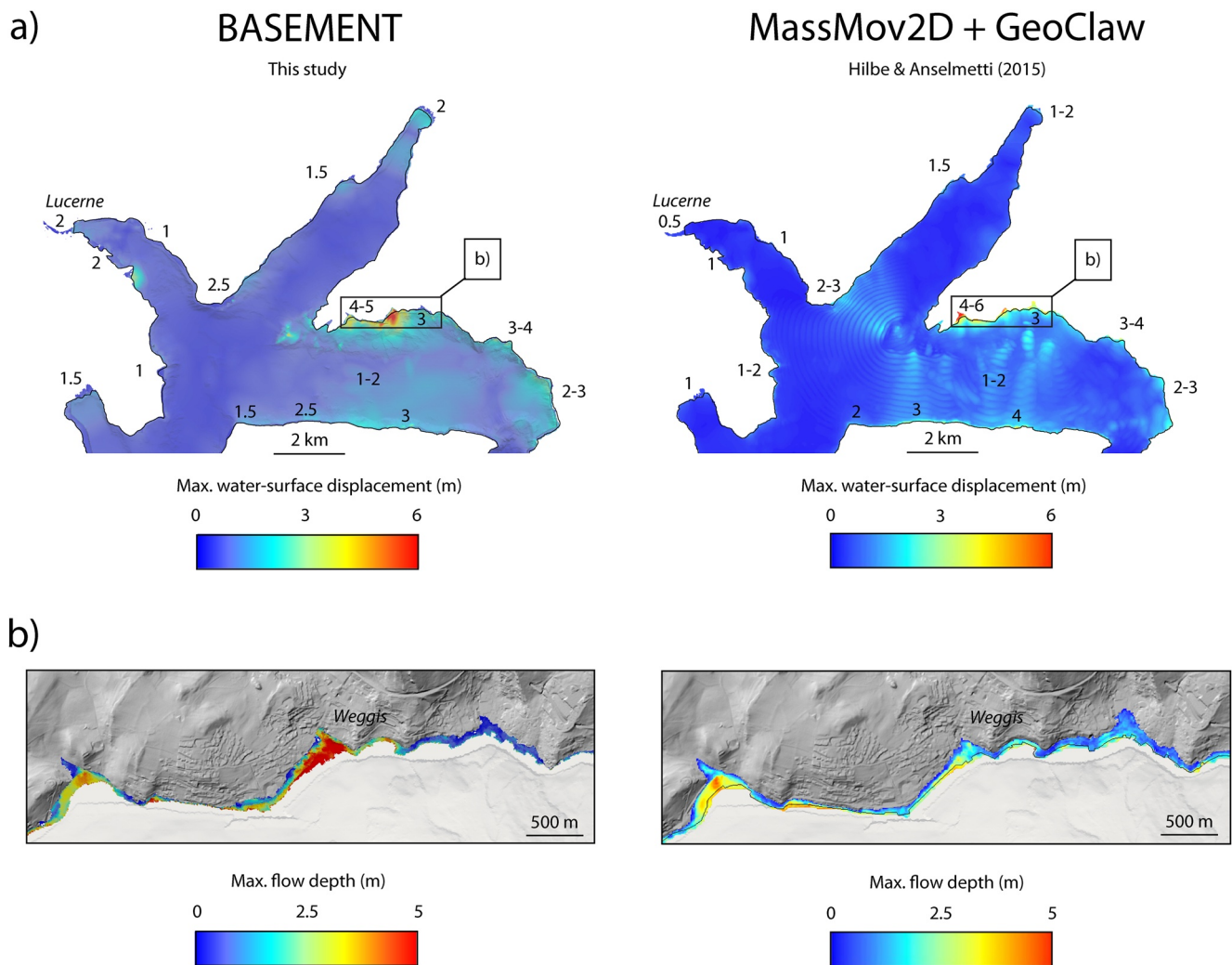


Figure 9. Validation and comparison of the Weggis-slide tsunami simulation computed with BASEMENT (left) with the simulation of Hilbe and Anselmetti (2015) based on MassMove2D and GeoClaw (right). (a) Maximum water-surface displacement and (b) max. flow depth at Weggis, proximal to the tsunami source in the Vitznau Basin, Lake Lucerne.

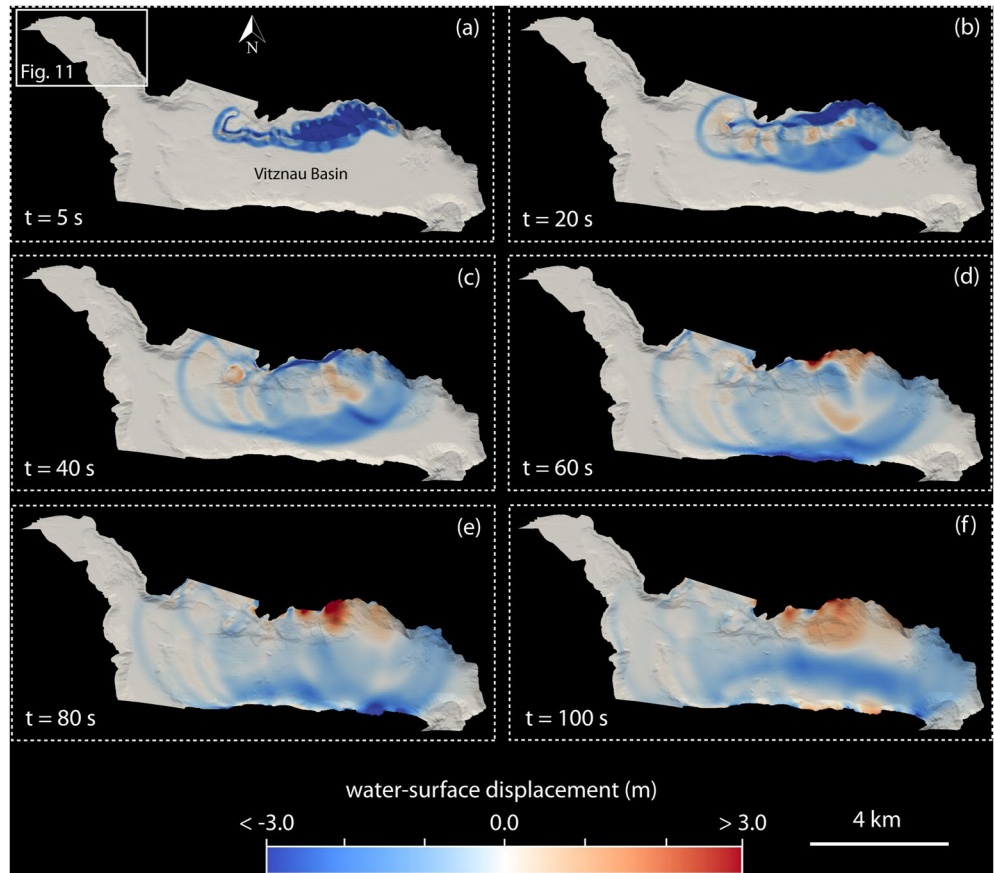


Figure 10. Time snapshots of the computed tsunami propagation and water-surface displacement (-3 to $+3$ m with respect to the lake at rest) of the 1601 CE Weggis slide (simulation LU18-S4) within the first 100 s after the simulated subaqueous mass movement. Tsunami propagation simulation at 5 s (a), 20 s (b), 40 s (c), 60 s (d), 80 s (e), and 100 s (f) after triggering.

(Figure 10c). Simultaneously, the tsunami waves propagate toward the center of the Vitznau Basin (Figures 10b and 10c) and reach the steep southern shore within 60 s (Figure 10d), where the wave is reflected. Along the northern and southern shorelines (Figures 10e and 10f) and in the center of the basin (Figure 10f), a complex wave pattern is formed from the superposition of reflected waves.

Figure 11 shows four time-snapshots of the computed tsunami propagation and water-surface displacement in the Lucerne Bay. A train of waves arrives in the narrow and shallow bay with an initial wave trough and a water-surface displacement of up to -1 m after 410 s (Figure 11a). At the transition from the deeper to the shallow-water area of the Lucerne Bay, a dominant flow direction toward the wave trough can be observed (Figure 11a) with a flow-velocity magnitude greater than 2 m s^{-1} (Figure 12). At ~ 550 s (Figure 11b) the first wave crest with a water-surface displacement between $+0.2$ and $+0.5$ m propagates along the bay with a flow-velocity magnitude of 2.2 m s^{-1} at the wavefront. The second wave trough is characterized by a complex and heterogeneous flow field, which propagates along the bay at ~ 755 s (Figure 11c). The wave trough with a water-surface displacement of -1 m is followed by a wave crest of $+0.5$ m with a dominant flow direction toward the sediment-core locations (Figure 11d) and a max. flow-velocity magnitude of ~ 2.4 m s^{-1} at gauge 2 and ~ 0.9 m s^{-1} at gauge 3 (Figure 12b). The third wave has a smaller water-surface displacement than the first two, but flow-velocity magnitudes at gauges 2 and 3 are similar to the first two waves (Figure 12b). The third wave is followed by subsequent waves with smaller water-surface displacements and flow-velocity magnitudes (Figure 12).

4.5.3. Sensitivity Analysis of the Bed Shear-Stress

To determine the dependency and robustness of the computed flow parameters, a sensitivity analysis of the bed roughness (k_b) was performed. Six scenarios were simulated with different bed-roughness values ranging from 0.0002 to 0.1 m (Table 3). The sensitivity of the bed roughness on the dimensionless bed shear-stress (θ) was

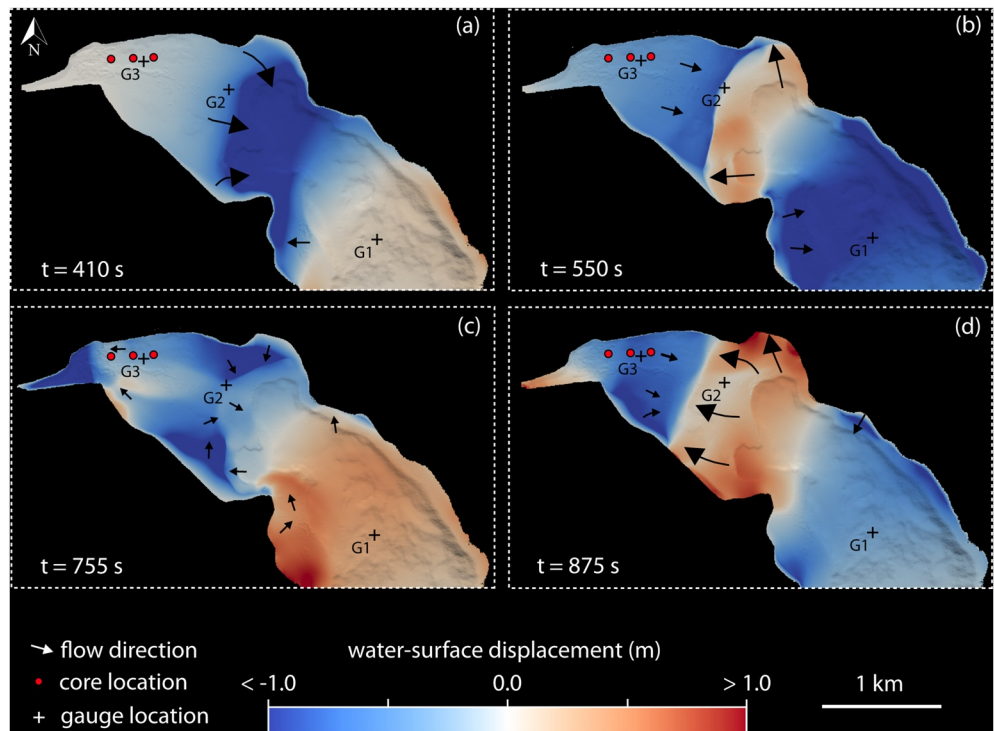


Figure 11. Time snapshots of the computed tsunami propagation and water-surface displacement of the 1601 CE Weggis slide (simulation LU18-S4) in the Lucerne Bay. The water-surface displacement (-1 to $+1$ m) and flow-velocity direction (indicated by black arrows, size relates to the flow velocity) are shown at four distinct time steps (410 (a), 550 (b), 755 (c), and 875 s (d)). Time series of water-surface displacement and flow-velocity magnitude at the virtual gauges 1, 2, and 3 (black crosses) are plotted in Figure 12. Sediment-core locations (red dots) are shown in the map.

evaluated by simulations computed with different bed roughness values between 0.0002 and 0.1 m, keeping fluid density (1 g cm^{-3}), sediment density (2.65 g cm^{-3}), and sediment porosity ($0.4 \text{ vol}\%$) constant (Table 3).

The analysis of the computed data in gauge time series and spatial variability indicate that the applied bed roughness has a strong effect on the dimensionless bed shear-stress. However, water-surface displacement, flow-velocity magnitude, and specific discharge are hardly affected. For example, flow-velocity magnitude has a variance

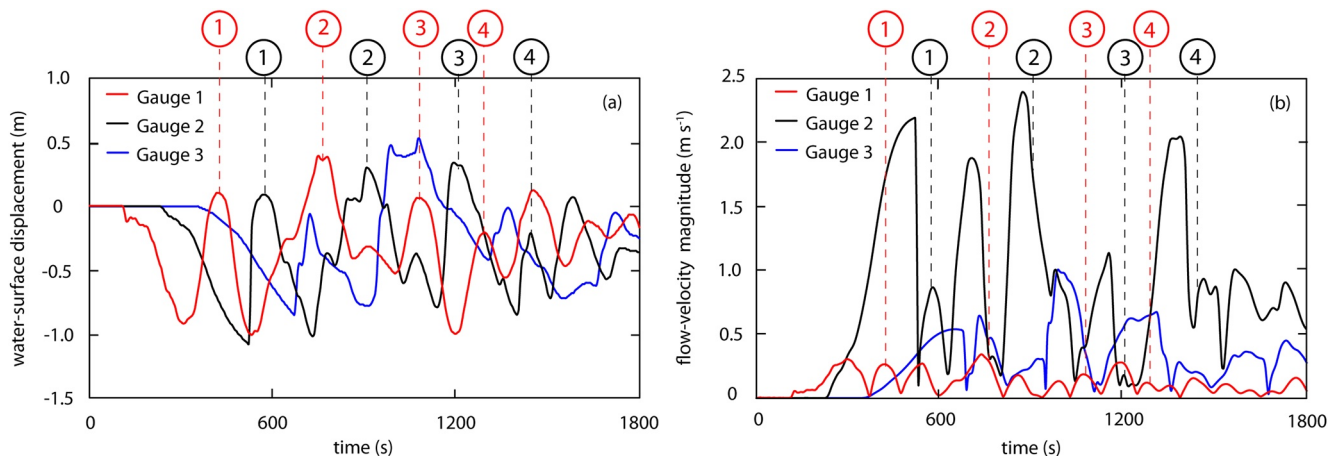


Figure 12. Time series of water-surface displacement (a) and flow-velocity magnitude (b) at the virtual gauges 1 (red), 2 (black), and 3 (blue) of the simulation LU18-S4. See Figures 2 and 11 for the gauge location. Wave numbers (encircled number) are indicated for direct visualization at gauge 1 (red) and 2 (black).

Table 3

Sensitivity Analysis of the Dimensionless Bed Shear-Stress to the Bed Roughness (k_b): Applied Bed Roughness in the Different Scenarios Computed With BASEMENT and the Calculated Area With a Dimensionless Bed Shear-Stress $\theta \geq 0.03$

	LU-S1	LU-S2	LU-S3	LU-S4	LU-S5	LU-S6
Bed roughness k_b (m)	0.0002	0.001	0.01	0.02	0.06	0.1
Area with $\theta \geq 0.03$ (10^6 m ²)	0.20	0.28	0.38	0.43	0.52	0.57

of less than 10% within the range of the different simulations at gauge locations. Whereas the computed dimensionless bed shear-stress is strongly influenced by the applied bed-roughness coefficient as shown in Figure 13.

The max. dimensionless bed shear-stress computed at the gauge locations range from 0.0001 to 0.0003 at gauge 1, 0.01 to 0.03 at gauge 2, and 0.001 to 0.003 at gauge 3 (Figures S1, S2, and S3 in Supporting Information S1). From the map-based analysis, it is evident that the highest observed max. dimensionless bed shear-stresses are most pronounced along the shoreline and in the shallow area at the transition from the deep to shallow water in the Lucerne Bay (Figure 13). The area with a max. dimensionless bed shear-stress $\theta \geq 0.3$ ranges from 0.2 to 0.6×10^6 m² for the various simulated bed-roughness coefficients (Table 3). See Movie S2 in Supporting

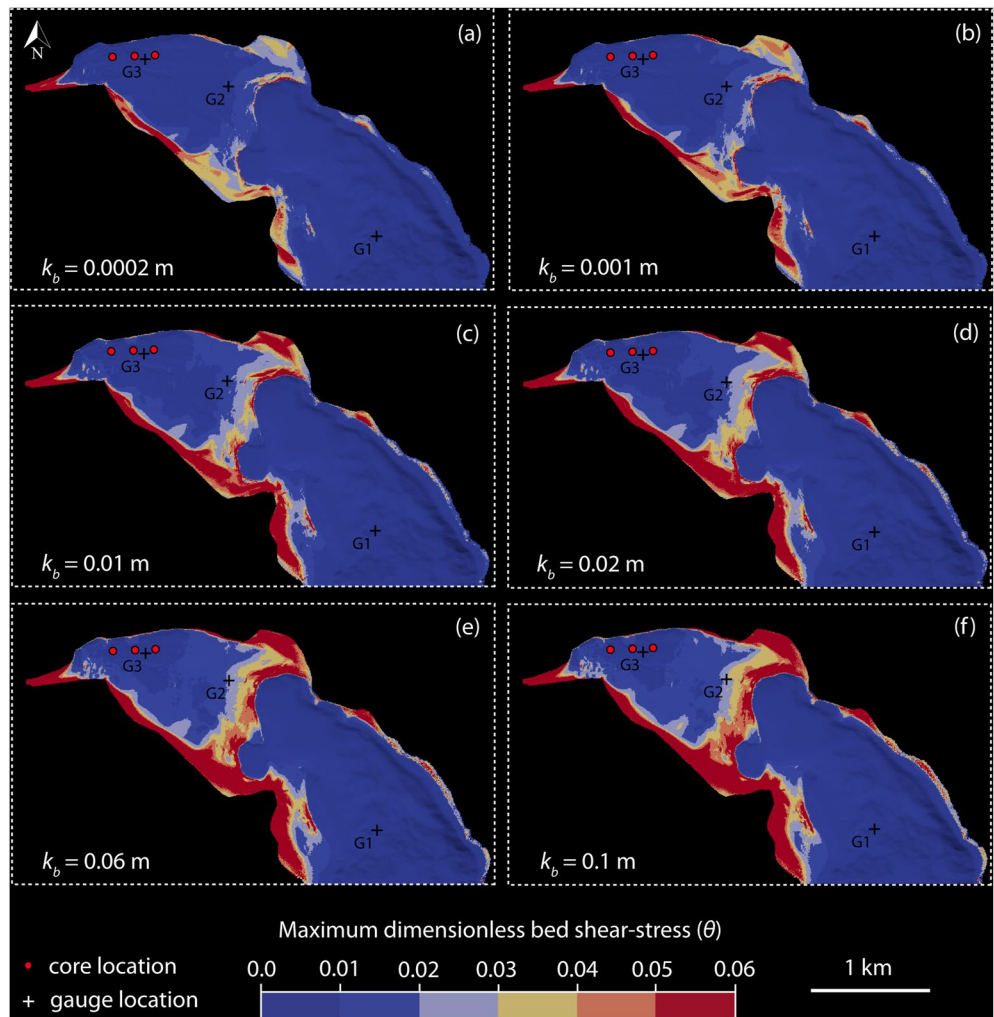


Figure 13. Results of the sensitivity analysis of bed roughness to the dimensionless bed shear-stress. The max. dimensionless bed shear-stress reached in each computational cell throughout the simulated time is shown for the simulation with different bed roughness ($k_b = 0.0002$ m (a); $k_b = 0.001$ m (b); $k_b = 0.01$ m (c); $k_b = 0.02$ m (d); $k_b = 0.01$ m (c); $k_b = 0.02$ m (d); $k_b = 0.1$ m (f)). Sediment-core (red dots) and gauge (black crosses) locations are shown on the map.

Information S1 for the animation of the dimensionless bed shear-stress evolution in the Lucerne Bay of simulation LU-S4.

5. Discussion

5.1. Depositional History

5.1.1. Unit 1: Dense—Cohesive Silty Clay

The lowermost Unit 1, characterized as a dense, cohesive, light-gray clay to silt deposit has been previously described in other sediment cores in the area (Keller, 2021). These deposits are interpreted as glaciolacustrine sediments deposited during an early lake phase (Keller, 2021).

The Reuss Glacier started to retreat around 22 kyr BP (Reber et al., 2014) and the northern alpine foreland in Switzerland became completely ice-free by 18 kyr BP (Ivy-Ochs et al., 2004). Nearby Lake Rotsee (Figure 2a) was ice-free before 18 kyr BP and its lowermost sediments contain terrestrial plant remains radiocarbon dated to at least 18.3 kyr cal BP (Ammann & Lotter, 1989). Based on drill cores and radiocarbon dating, Lucerne Bay was filled up with sediments to a level of 422 m asl by 14.7 kyr cal BP (Keller, 2021). The fine-grained, cohesive sediment originates from the retreating Reuss Glacier and probably corresponds to rock flour delivered by glacial runoff distal to the ice-contact. The unevenly occurring, cm-thick graded sandy layers probably correspond to distal glacier-fed episodic inter- and/or underflows in a glaciolacustrine system. Though there are a few modern studies focused on paleo-glaciolacustrine microfacies, the comparison with sedimentological models is limited (Palmer et al., 2019).

Sedimentary Unit 2 overlies Unit 1 discordantly and was radiocarbon dated to 1174–1277 cal CE, suggesting a hiatus of several 1,000 years. The hiatus is probably caused by the incision of the eroding outflowing Reuss River during lake-level low stands. Keller (2013) suggests a subsequent lowering of the lake level from 432 m asl around 15 kyr BP to 428.6 m asl in the Neolithic Age (between 7 and 4 kyr BP) and rose again to 429.5 m asl during the Roman Period. The subsequent lowering of the lake level caused a regressive phase and a displacement of the shoreline ~1.5 km eastward to the transition from the deep to the shallow water of the Lucerne Bay (Figure 2). During this phase, the River Reuss probably meandered through a marshy alluvial plain that established along the shallow-water area of the present-day Lucerne Bay (Keller, 2021).

5.1.2. Unit 2: Light Brown Gyttja

With the construction of water mills in the thirteenth century at the outflow of the lake, lake level was stabilized at today's level and Lucerne Bay became submerged (Keller, 2021). This early stabilized lake-level phase corresponds to the deposition of Unit 2 that is radiocarbon dated to 1174–1277 cal CE. The unit consists of organic-rich deposits with limited carbonate content and variable thickness along the coring transect (Figure 5). These organic-rich deposits (gyttja) suggest high primary production in a nutrient-rich environment (Ismail-Meyer et al., 2018). It consists largely of a soft accumulation of residues from aquatic organisms (e.g., diatoms, plant tissues, and feces) and partially decomposed terrestrial plant remains. The accumulation of organic matter from suspension at the sediment-water interface occurs under anaerobic conditions (Ismail-Meyer et al., 2018), which is favorable during a eutrophic lake state. Sewage from the growing city likely caused the eutrophication in Lucerne Bay.

5.1.3. Unit 3: Normally Graded Sand to Silt

The normally graded Unit 3 overlies Unit 2 with a sharp basal contact, indicating an abrupt depositional event in Lake Lucerne. The narrow radiocarbon age range (1306–1437 cal CE) with minor age reversals (Figure 6) supports the hypothesis of abrupt deposition. Sedimentologically, Unit 3 is characterized by a fine sandy base with coarse fragmented carbonate shell fragments at the base that gradually fines upward to a poorly sorted fine silt (Figures 5 and 8). A clear shift in the grain-size distribution is observable in Core LU18-2 at depths of 95, 60, and 55 cm (Figure 8). The lowermost 7 cm have a well sorted grain-size distribution with a D_{50} of 90–180 μm . The overlying 45 cm (core depth: 60–95 cm) have a well sorted grain-size distribution with a D_{50} of 27–75 μm , whereas the uppermost 23 cm (core depth: 37–60 cm) are moderately to poorly sorted with an apparent bimodal grain-size distribution (Figure 8). The XRF Si/Al ratio correlates well to the grain-size distribution in Unit 3. The clear shift at 60 and 55 cm from well sorted to moderately and poorly sorted, respectively, is also expressed (Figure 6).

Therefore, the Si/Al ratio is likely an indicator for the grain-size variability at the mm-scale. However, larger variations may also result from an undulous scanning surface of the fine sandy sediment section. Consequently, the grain-size indicator must be used with caution. However, it supports the LDA grain-size measurements.

The textural observations made in Unit 3 clearly indicate a single depositional event. Normally graded sedimentary beds have been described for rapid deposition in high-energy flows such as tsunamis and turbidity currents (Jaffe et al., 2011; Kuenen & Menard, 1952; Middleton, 1967) and depositional environments where transport energy decreases with time (Kuenen, 1953). Turbidity currents generated by mass movements in the flat and shallow Lucerne Bay seem unlikely. However, the gradual upward decrease in grain size is indicative of deposition from suspension (Jaffe et al., 2012). This specific type of normal grading is termed suspension grading (Jaffe et al., 2012) and is primary caused by the settling velocity of the particles. Thick, normally graded deposits have been reported from the nearshore (Sakuna et al., 2012; Tamura et al., 2015) and onshore environments (Jaffe et al., 2012 and references therein) deposited by the inundation and backwash of marine tsunamis. For example, Kempf et al. (2015) have observed normally and multiple graded sand deposits with mud caps and variable thicknesses (5–60 cm) in two Chilean coastal lakes, that record the local inundation of the 1960 CE Great Chilean Earthquake tsunami. Of the few shallow-water tsunami deposits studied worldwide, several authors have described sharp lower and/or upper sedimentary contacts (Abrantes et al., 2008; Goodman-Tchernov et al., 2009; Sakuna et al., 2012; Smedile et al., 2020; Van den Bergh et al., 2003), as observed at the basal contact of Unit 3. In Lake Sils, Nigg, Wohlwend, et al. (2021) observed thick, normally graded sand deposits that were likely formed by the backwash currents of a prehistoric lake tsunami.

Horizontally bedded wood fragments that are more abundant in the upper part of the unit indicate a terrestrial sediment component, possibly caused by tsunami inundation and backwash. The increases in TOC and C/N ratio from 15 to 20 in the uppermost 20 cm of the event deposit (Figure 6) supports the observation of an increase of wood fragments in the upper part of the unit. Terrigenous components such as coarse organic material (e.g., wood fragments) and anthropogenic artifacts (e.g., brick pieces) were observed in other tsunami deposits, such as the 2004 CE Indian Ocean tsunami in sediment cores from the continental shelf in the Andaman Sea, Thailand (Sakuna et al., 2012). Side-scan sonar surveys revealed tree trunks aligned perpendicular to post-tsunami sand ripples from the same event in ~15 m water depth at Lhog Ngam, Western Banda Aceh, Sumatra, Indonesia (Paris et al., 2010).

5.1.4. Unit 4: Lacustrine Carbonate

Uppermost Unit 4 represents a modern lake system with high endogenous carbonate production in an oligotrophic lake (Bossard et al., 2001) that became more nutrient-rich during a period of eutrophication in the 1970s–1980s (Thevenon et al., 2012). The high magnetic susceptibility is attributed to combustion particles associated with the development of steam navigation on Lake Lucerne from the beginning of the late 1830s (Figure 6). A radiocarbon date with a modern age (Table 1) likely indicates reworking of the uppermost sedimentary facies by storms and human activities (e.g., steam navigation and recreational boating).

5.2. Age of Unit 3

Radiocarbon ages obtained from conifer needles and leaf fragments in Unit 3 yield a max. age of 1326 cal CE (Table 1) for the deposition of the unit. Although the sedimentological characteristics of the event provide a good reasoning for the 1601 CE Lake Lucerne tsunami as the underlying cause, the radiocarbon ages are ~300 to 200 years older than the historically reported event. The narrow range of radiocarbon ages obtained from Unit 3 together with the grain-size pattern suggests with high confidence that the unit was deposited in a single event. It is reasonable to examine contemporaneous events as the cause for the deposition. Therefore, four exceptional historical events that fall within this period are discussed below: (1) the 1356 CE Basel earthquake, (2) the historical lake-level regulation in the thirteenth and fourteenth centuries, (3) a 1,000-year flood event that occurred in 1342 CE in Central Europe and (4) the 1601 CE Lake Lucerne tsunami.

1. The 1356 CE Basel earthquake, with a reconstructed moment magnitude M_w of 6.7–7.1 and an epicentral macroseismic intensity of I_0 IX, was one the most damaging earthquake in Europe during historical times (Fäh et al., 2009). Although the event caused intensities of up to VIII within a radius of 30 km (Fäh et al., 2009), no secondary effects were historically reported from the 75 km distant Lake Lucerne. This is further supported by the absence of mass-movement deposits and in situ soft-sediment deformation structures in lake sediments

- of Central Switzerland from this event (Monecke et al., 2004). Although the historically reconstructed macroseismic intensity at Lake Lucerne might be approximately in the same range as the intensity caused by the 1601 CE earthquake (Monecke et al., 2004; <http://www.seismo.ethz.ch/en/knowledge/earthquake-country-switzerland/historical-earthquakes/basel-1356/>), shaking was obviously not high enough to trigger mass movements voluminous enough to generate large water displacements in Lake Lucerne.
2. With the establishment of the City of Lucerne in the thirteenth century and constructions of mills at the lake outlet, lake level was artificially stabilized at ~432.5 m asl (Keller, 2021). Previously, lake level was generally lower at 429 m asl during the Roman Period and between 428.6 and 429.5 m asl in the Neolithic Age (between 7 and 4 kyr BP) (Keller, 2021; Michel et al., 2012). During this time, the Lucerne Bay may have been an extended coastal wetland with marsh vegetation and only partially submerged. With the artificial regulation of the lake level the Lucerne Bay became completely submerged. In sedimentary basins, transgressive phases generally form characteristic reverse graded sedimentary successions (Boggs, 2014). Furthermore, submergence may cause sediment erosion, transport, and redistribution along the shoreface (Kraft, 1971). However, it is hypothesized that in the Lucerne Bay, more specifically in the east-west oriented depression (Figure 2), sediment availability and sediment transport are limited during a relatively gentle rise of the lake level. Moreover, radiocarbon dates and textural observations of Unit 3 are indicative for an abrupt depositional process, whereas the transgression probably lasted several decades. Therefore, the submergence of the Lucerne Bay in the thirteenth century is unlikely the origin of Unit 3.
 3. Central Europe was hit by an unprecedented flood event in 1342 CE (Bork & Piorr, 2000; Kiss, 2009). The harsh winter with abundant snow and the very rainy summer as well as autumn caused three major floods in large parts of Central Europe (Kiss, 2009). The summer flood, known as the St. Mary Magdalene's flood, was an extreme, millennial flood event with disastrous consequences (Kiss, 2009). Certain historical chronicles also mention the following year (1343 CE) as another high-precipitation event with persistent rainfall in Switzerland, Germany, and the Carpathian Basin that resulted in catastrophic flooding (Camenisch, 2019; Glaser, 2008; Kiss, 2009; Pfister & Hächler, 1991). Unusual high-water levels were reported from several Swiss freshwater basins such as Lake Zurich, Lake Constance, and Lake Lucerne (Camenisch, 2019; Pfister & Hächler, 1991). Low-lying parts of the City of Lucerne were extensively flooded in 1343 CE (Schaller-Donauer, 1937). A church located about 150 m south of the outflowing Reuss River was only accessible by boat (Schaller-Donauer, 1937). Siegenthaler and Sturm (1991) attributed a thick turbidite deposit in the south-eastern basin of Lake Lucerne to the event, which was caused from the high discharge of the Reuss River. Although, the thickness distribution is largely unknown, it is the thickest and coarsest turbidite deposit observed in the Uri Basin during the last 1,000 years (Siegenthaler & Sturm, 1991). Flood-generated turbidites are generally characterized by a normally graded deposit with a distinct fine-grained top, referred to as clay cap (Gilli et al., 2013; Mulder et al., 2001). The event deposit may contain multiple graded layers and/or an inversely graded base (Gilli et al., 2013; Wirth et al., 2013). This succession is directly related to the waxing and waning of the hydrologic sequence of river discharge during heavy precipitation events (Gilli et al., 2013; Mulder et al., 2001). The thickness distribution strongly depends on the catchment area and in some cases on the flood intensity but is generally in the range of several cm (Wilhelm et al., 2013). This contrasts with observations made in the sediment cores analyzed in our study. The event deposit is characterized by a 60-cm thick, normally graded siliciclastic sand unit with coarse shell fragments at the base (Figure 8). Although the Krienbach River drainage basin caused repeated flooding in Lucerne City during the historic period, these events were not observed in the studied sediment record. Nonetheless, the 1342/1343 CE floods likely delivered large sediment volumes that were resuspended and transported during the 1601 CE tsunami.
 4. The 1601 CE Lake Lucerne tsunami is clearly an unprecedented natural hazard event in Central Switzerland with profound consequences as described in more detail above (Section 2.1). The M_w 5.9 earthquake with an epicentral intensity of VII (exceeding VI in large parts of the lake; Monecke et al., 2004) triggered multiple subaqueous mass movements and a subaerial rockfall that impacted the lake surface (Hilbe & Anselmetti, 2015; Keller, 2017; Schnellmann et al., 2006; Schwarz-Zanetti et al., 2003). These mass movements generated a basin-wide tsunami with run-up heights of several meters and inundation of coastal plains by several hundred meters (Cysat, 1969; Hilbe & Anselmetti, 2015) and entire shoreline sections submerged into the lake (Cysat, 1969). At the lake outlet, oscillation of the entire lake by several meters was recognized for several hours after the event, causing the River Reuss to flow back into the lake and partially drained the riverbed (Cysat, 1969).

5. Tsunami deposits are generally dated directly and/or indirectly using material from within and/or from above and below the event deposit (Ishizawa et al., 2020). In this study, we took samples for dating above, within, and below the event deposit using short-lived terrestrial plant remains. The event underlying Unit 2 was radiocarbon dated to 1174–1277 cal CE (Table 1). The event overlying Unit yields a modern radiocarbon age. Four samples were radiocarbon dated from within the event deposit and range in age between 1306 and 1442 cal CE. However, dating of reworked material from within a tsunami deposit are considered a maximum age because it consists of reworked sediment deposited prior to the event (Ishizawa et al., 2020). Thus, the series of too-old ages from the event deposit is consistent with other studies on dating tsunami deposits and does not argue against the 1601 CE Lake Lucerne event. The youngest dated sample with an age of 1326–1442 cal CE corresponds to a maximum age for Unit 3 of 1326 cal CE, which likely represents sediment previously deposited in Lucerne Bay during the 1342/1343 CE floods, and resuspended and transported during the 1601 CE tsunami. Remarkable sediment remobilization by the 2011 CE Indian Ocean tsunami, for instance, was observed from bathymetric changes at Kirinda Harbor, Sri Lanka (Goto, Takahashi, et al., 2011). Substantial remobilization and redeposition of pre-event sediments along the shallow water and onshore is likely an important process in freshwater tsunamis too. Therefore, we numerically simulated the Weggis slide with BASEMENT and investigated wave velocity, flow field vectors, and the dimensionless bed shear-stress to estimate the erosional potential in Lucerne Bay.

5.3. Numerical Simulation

Subaqueous mass movements are highly dynamic processes that are very complex to simulate adequately numerically (Behrens et al., 2021; Urlaub et al., 2013). The characteristics of subaqueous mass movement-generated tsunamis strongly depend on the initial stages of the failure (e.g., mass-movement volume, initial acceleration, maximum velocity, water depth, and slide dynamics) (Harbitz et al., 2006; Løvholt et al., 2015; Watts, 1998). Failures in the shallow water induce typically tsunamis with large run-up heights close to the mass movement (Løvholt et al., 2015; Okal & Synolakis, 2004). However, Løvholt et al. (2017) have found evidence that some giant landslides may not have produced tsunamis. The temporal evolution of mass movement is critical. Multi-stage retrogressive failures, separated by several days, will have lower tsunamigenic potential than a single-block failure (Hunt et al., 2011). This highlights the importance of single- and multistage-slide dynamics. The simultaneous failure of multiple subaqueous mass movements greatly increases complexity and uncertainty of numerical simulations.

The tsunami triggering mechanism used in this study greatly simplifies the natural processes of subaqueous mass movements. The Weggis slide was simulated by an instantaneous collapse of 5 m along the identified failure area (Figure 2) corresponding to a worst-case scenario. Anyhow, the computed results are reasonable (e.g., water-surface displacement, inundation distance, and flow depth) and compare well with the historic reports of the 1601 CE event (Cysat, 1969) and the simulation of Hilbe and Anselmetti (2015). Therefore, we are confident that the strong simplification of the tsunami triggering mechanism can be well used for the identification of potential sediment source in Lucerne Bay. However, overestimates of water-surface displacement and run-up proximal to the tsunami source must be considered. Moreover, since the historical 1601 CE Lake Lucerne tsunami was generated by multiple simultaneously failed subaqueous mass movements, complex wave interaction likely occurred. However, this phenomenon was not included in this study. Beyond that, this approach could be used for a rapid tsunami hazard assessment for subaqueous mass movement-generated tsunamis in lakes (Strupler, Anselmetti, et al., 2020).

Tsunamis generated by earthquakes and subaqueous mass movements are characterized by a series of propagating waves that can cross entire oceans within hours (Bryant, 2014). From historical reports (e.g., 1998 CE Papua New Guinea), it is well known that coasts are usually hit by a wave train, with the first wave having a lower amplitude than subsequent waves (Davies et al., 2003). The arrival of the first wave may be characterized by a retreat of the water (draw down), exposing the seabed (Röbke & Vött, 2017). The drawback and the propagating wavefront will collide and form a wave with sharp drop downward, resulting in a wave break that rapidly approaches the shoreline (Lampela, 2019). However, depending on the position with respect to the tsunami source, sometimes the arrival of the wave train may also be characterized by an approaching wall of water (Bryant, 2014). This behavior is well reproduced by our numerical simulation with BASEMENT. After tsunami generation, a wave train propagates along the Vitznau Basin (Figure 10). The arrival of the tsunami in the Lucerne Bay is characterized by

a drawback of the water (Figures 11a and 11b). The collision with the propagating wave train forms a steep wave-front (Figure 11b). Moreover, as confirmed by general observations of tsunami behavior (Davies et al., 2003), the first wave is lower than the subsequent waves. This can be observed from the water-surface displacement of individual wave numbers in the time series of gauge data (Figure 12). From the sensitivity analysis, it is evident that the flow parameters (water-surface displacement, specific discharge, and flow-velocity magnitude) in deep water (gauge 1) are almost not influenced by different bed roughness values (Figure S1 in Supporting Information S1). In contrast, in shallow water these effects are already pronounced at the arrival of the first wave (Figures S2 and S3 in Supporting Information S1). However, after 1,000 s of computation time, slight differences appear at gauge 1, due to reflection and backwashes in shallow water, where bed roughness influences the flow parameters.

5.4. Sediment Source, Erosion, Transport, and Deposition

5.4.1. Erosion, Maximum Dimensionless Bed Shear-Stress, and Bed Roughness

The max. dimensionless bed shear-stress is the key value that defines whether sediment is eroded by flow events (Van Rijn, 2007). The dimensionless bed shear-stress reached during the propagation of the tsunami generated by the 1601 CE Weggis slide (Figure 1) in Lucerne Bay was numerically simulated with BASEMENT to better understand the erosion and mobilization potential of the tsunami waves. For this purpose, the influence of bed roughness on the incipient motion of particles was considered. Sediment may be eroded when the effective dimensionless bed shear-stress is larger than the dimensionless critical bed shear-stress, that is., $\theta > \theta_{cr}$ (Choi & Kwak, 2001). However, critical dimensionless bed shear-stress depends on the grain-size distribution and cohesion of the sediment bed (Houwing & Van Rijn, 1998). For the given situation, the threshold for incipient motion was chosen at $\theta = 0.03$, which has been previously suggested to be a reasonable number based on empirical experiments (e.g., Shields, 1936; Houwing & Van Rijn, 1998). As soon as the threshold for incipient motion is reached, sediment particles may be entrained by the flow (Van Rijn, 2007). Once sediment particles are set in motion, less energy is generally required to keep particles in motion after entrainment (Boggs, 2014).

The applied physical bed roughness (k_b) varies from 0.0002 to 0.1 m (Figure 13), which is a reasonable range from grain roughness to total physical bed roughness (Houwman & Van Rijn, 1999). Total physical bed-roughness, and thus effective dimensionless bed shear-stress, may be influenced by sedimentary bed forms (e.g., ripples and dunes), superimposed bed forms (e.g., megaripples), grain-size distribution and packing, mineralogical sediment composition, and the presence of an organic biofilm on the lake bed (Van Rijn, 2007). Therefore, accurate estimates of total physical bed roughness are difficult to obtain. Houwman and Van Rijn (1999), for example, have found that physical bed roughness of 0.1 m gives best agreement between measured and predicted current velocities in the North Sea at water depths of 5–10 m and a D_{50} of 200 μm . Thus, considering the above-mentioned factors and that surf beats are less expressed in the Lucerne Bay than at the North Sea coast, physical bed roughness of 0.02–0.06 m is a reasonable value for the given situation (Figures 10d and 10e).

Considering the above limitations in the estimation of incipient motion, our simulation shows large areas with a dimensionless bed shear-stress $\theta \geq 0.03$ (Figure 13). This indicates large amounts of sediment that may have been resuspended and transported by the main wave pulses in shallow Lucerne Bay. The areal extent of max. dimensionless bed shear-stress $\theta \geq 0.03$ computed for different physical bed-roughness is in the order of $0.2\text{--}0.6 \times 10^6 \text{ m}^2$ (Figure 14a). A very rough estimate of the erosion volume can be calculated based on the assumption of a homogeneous erosion thickness on the area with $\theta \geq 0.03$. The calculated volume of eroded material for an erosion thickness between 0.02 and 0.2 m is in the order of $4\text{--}11.5 \times 10^4 \text{ m}^3$ (Figure 14), indicating that the 1601 CE Lake Lucerne event likely eroded and remobilized large sediment volumes in the Lucerne Bay. Significant reworking is further supported by radiocarbon ages of up to 300 years older than the tsunami event as determined in the event bed.

5.4.2. Sediment Source

The numerical simulations clearly indicate where and when the tsunami waves cause bed shear-stress in the Lucerne Bay capable of substantial sediment erosion and mobilization (Figure 13, Movie S2 in Supporting Information S1). Erosional forces are pronounced in the shallow-water area of the geomorphological obstacle that mark the transition from the deeper to the shallower area of the Lucerne Bay and along the lake shore, as indicated by the computed max. dimensionless bed shear-stress (Figure 13). These areas are likely the sediment source for remobilized sediment particles during the 1601 CE tsunami propagation in Lucerne Bay. Another important

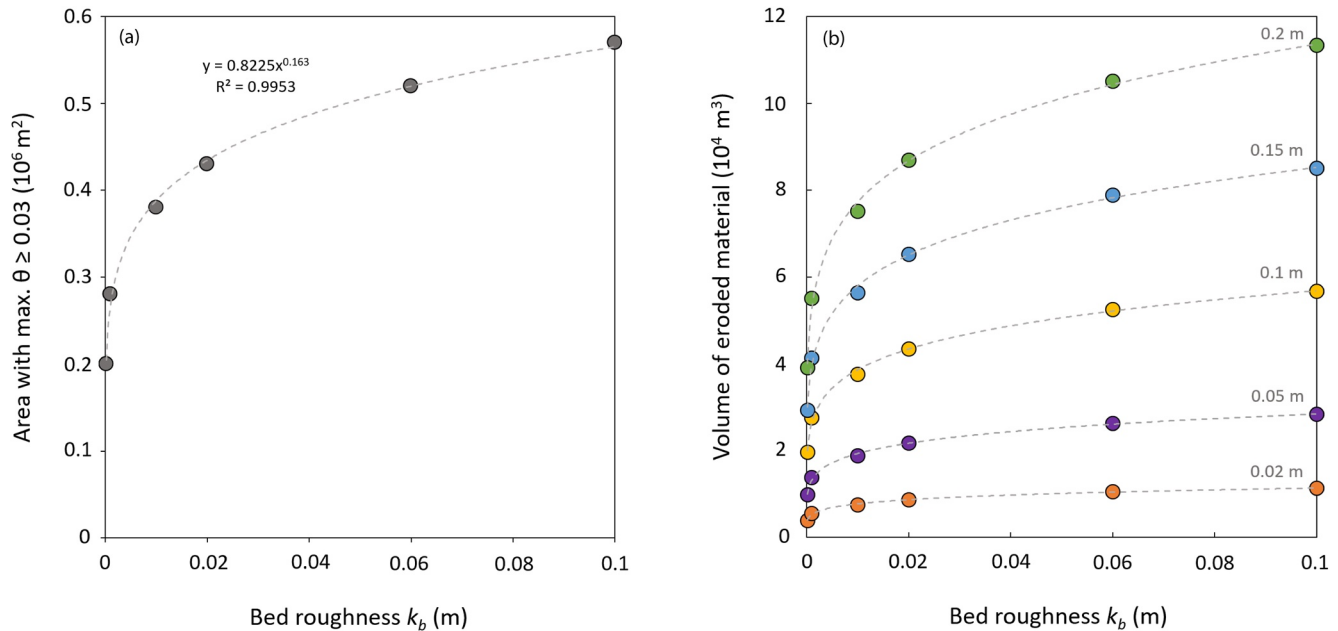


Figure 14. (a) Mapped area with a max. dimensionless bed shear-stress $\theta \geq 0.03$ reached, computed with different bed roughnesses k_b , (b) Estimation of remobilized sediment volumes with different homogeneous erosional thicknesses and bed roughnesses k_b .

sediment source is the lake shore, where predominantly siliciclastic sand is found (e.g., lake-bed sediment Sample LS-3). At these locations, constant wave motion leads to sandy-dominated surface sediments from winnowing of fines.

The enrichment of horizontally embedded wood fragments toward the top of the event unit indicates a terrestrial sediment source. In the near shore or subaerial areas, wood is abundant and can be mobilized by the wave. Due to its low density, when compared to minerogenic particles, mobilized wood fragments eventually accumulate in the upper part of the event deposits. In this study, we did not further characterize and investigate the overland flow in the Lucerne Bay area, mainly due to the heavily artificially altered shoreline. A historical reconstruction of shore-line topography was nearly impossible within the objectives of this study. However, we corrected for large shoreline modifications performed in the last century (Figure 2). In addition to exposed shore areas, a terrestrial component may also originate from the tributaries of the Würzenbach and Krienbach. The distinction of the subaqueous from the subaerial source, however, is not straight forward. Goto, Takahashi, et al. (2011) found through repeated bathymetric surveys that the amount of sediment mobilized by tsunamis is much more substantial in the nearshore than onshore. Therefore, we propose that the subaqueous sediment source is more dominant compared to the onshore, which is also supported by the numerical simulation of the max. dimensionless bed shear-stress.

5.4.3. Sediment Transport and Deposition

The sediment transport toward the coring site can be observed by visualizing flow-velocity vectors indicating the sediment-transport direction (Figure 11). Three main wave pulses propagate in Lucerne Bay in the first 30 min after the instantaneous simulated Weggis-slide collapse (Figure 11 and 12). During the first wave, a strong flow toward the wave trough is observable (Figure 11a). At this stage, sediment particles may be mobilized and brought into suspension. With the arrival of the second wave, particles are transported westward (Figure 11d). These main wave pulses have high flow velocities ($>2 \text{ m s}^{-1}$; Figure 12b) and specific discharges ($>4 \text{ m}^3 \text{ s}^{-1}$; Figures S1, S2, and S3 in Supporting Information S1) that are capable to transport large amounts of sediment from the areas with high bed shear-stress, where erosion occurs, toward the coring location. Due to the geomorphological depression at the coring location (Figure 2b), flow velocity drops instantaneously, and sediments are likely deposited from suspension forming the normally graded event deposit. Historical reports document an oscillation of the entire lake with an initial amplitude of 1–2 m and a period of 10 min in the following hours and days after the event (Cysat, 1969). The oscillation of the water column was not included in our simulation. Therefore, the dimensionless bed shear-stresses generated by the motion are unknown. However, the persistent water motion might have

contributed to the sediment mobilization. The horizontally embedded wood fragments likely indicate continuous flow and deposition under these conditions.

The up to 60-cm-thick normally graded Unit 3 clearly indicates deposition from suspension. The shift of the entire distribution from coarser to finer sizes is a signature of sediment falling out of suspension (Jaffe et al., 2012). However, the thickness of suspension-graded portion of tsunami deposits is, however, typically 10 cm or thinner (Jaffe & Gelfenbaum, 2007). We suggest that the observed geomorphologic depression strongly influences the sedimentary architecture of the event deposit. Sediment convergence is situated at the coring location, where flow velocity abruptly decreases due to the depression in the lake-bed morphology (Figures 2b and 12b). Deposition from suspension-settling occurs as the flow wanes during the final stage of the event. However, several studies have observed evidence of bedload transport in the lower section of tsunami deposits (Jaffe et al., 2012; Nanayama et al., 2007). These textural characteristics include massive or inversely graded intervals, current ripples, and dunes (Jaffe et al., 2012; Nanayama et al., 2007). The absence of signatures of bedload transport in the 1601 CE Lucerne Bay tsunami deposit can be explained by several reasons. Sediment cores provide selective information on the spatial variability of sedimentary deposits. Therefore, nonobservance of a certain feature is not an argument for its absence. Moreover, bedload transport accounts for less than 10% of the total tsunami-induced sediment-transport (Jaffe & Gelfenbaum, 2007). In addition, Jaffe and Gelfenbaum (2007) assumes that tsunami deposits reflect primarily suspended load transport when sediment transport is large. Grading is better developed when the sediment source is poorly sorted (Jaffe et al., 2012). This is consistent with our numerical simulation of the bed shear-stress, which gives an indication for the sediment source location. High bed shear-stresses are observed at the transition from the deeper to shallower Lucerne Bay, at the toe of the Würzenbach River Delta and along the lake shore (Figure 13). The latter two sites are characterized by moderate to poorly sorted sediment (Table 2; LS-3 and LS-4). These areas are likely the sediment source of the siliciclastic-rich normally graded Unit 3.

A depositional volume of $3.5 \times 10^4 \text{ m}^3$ is estimated from the thickness of Unit 3 in recovered sediment cores and spatial extend of contour line 426.6 m asl (Figure 2b; Table S3 in Supporting Information S1). This estimate fits in dimension with the proposed area of erosion and a homogeneous erosion thickness of at least 10 cm (Figure 14), explaining the ages of reworked particles that are $\sim 300\text{--}200$ years older than the event. However, it is unknown if and where the event deposit is also present along the shallow-water platform of Lucerne Bay or if it is spatially restricted to the geomorphologic depression. A more accurate estimation of eroded volume would be possible by using more sediment cores, ground penetrating radar, and a fully featured model for suspended-sediment transport. Such a model would allow for simulation of variable erosion related to the dimensionless bed shear-stress and provide more realistic transport of the sediment with the flow. However, many uncertainties may persist, for example, sediment-erosion thickness is likely not homogenous over the area and sediment erosion may be strongly influenced by local variations of sediment composition (e.g., mineralogy, grain-size distribution, and bed roughness).

6. Conclusions

An offshore event deposit was observed in sediment cores recovered along a transect across a depression in the shallow water of Lucerne Bay. The normally graded deposit with a thickness of up to 60 cm consists predominantly of siliciclastic sand-to silt-sized particles with increased amounts of coarse sand-sized carbonate shell fragments at the base. The deposit has a sharp basal contact with horizontally bedded organic, mostly woody particles that become more abundant in the upper part of the deposit. Radiocarbon dates of terrestrial plant macro-remains isolated from the clastic deposit yield ages in the range of 1306–1442 cal CE.

The sedimentary features clearly reflect deposition from a high-flow event, which we interpret to be the historically reported 1601 CE Lake Lucerne tsunami. This interpretation is supported by (a) the grain-size pattern of Unit 3 indicating deposition from suspension, (b) radiocarbon dating of the event deposit, which suggests significant sediment resuspension and transport of previously deposited sediment along Lucerne Bay, and (c) the performed numerical tsunami-wave propagation and dimensionless bed shear-stress simulation which provides a criterion for incipient motion and thus resuspension of sediment by the incoming waves.

The 1601 CE Lake Lucerne tsunami was simulated using the software BASEMENT considering an instantaneous collapse of the second largest subaqueous mass movement failed during the 1601 CE earthquake. Although mass-movement processes were simplified, the results obtained agree well with historical reports of the tsunami

event and previous numerical simulations. In addition to the simulation of the wave propagation, water surface-displacement, flow-velocity magnitude, and the dimensionless bed shear-stress was used to characterize and identify areas of tsunami-induced sediment erosion in the shallow water of Lucerne Bay. The simulated results clearly show that the critical dimensionless bed shear-stress is exceeded in large areas, where significant erosion must have occurred. Flow direction pointing from the erosional areas toward a geomorphological depression, where sediment cores were recovered along a transect.

Our study thus documents the high potential of combining sedimentological observations of event deposits with numerical simulations of wave propagation and dimensionless bed shear-stress. Based on the reconstructed process chain, we have successfully identified areas susceptible to tsunami erosion and deposition in shallow water based on sediment cores and numerical simulations. The proposed approach is not limited to lacustrine systems and mass movement-induced tsunami waves but can be applied to any basin where high-flow events occur.

Data Availability Statement

Data of core scans (MSCL and XRF), LDA particle-size measurements, virtual gauge used for the sensitivity analysis, interpolated lake bathymetry of the area used for numerical wave-propagation simulation, and coordinates of sediment cores, lake-bed samples, and virtual gauges used in this research are available from the data repository Pangaea (<https://doi:10.1594/PANGAEA.938716>) by Nigg, Bacigaluppi, et al. (2021). The BASEMENT software used in this research is described in detail in Vetsch et al. (2020) and Vanzo et al. (2021).

References

- Abrantes, F., Alt-Epping, U., Lebreiro, S., Voelker, A., & Schneider, R. (2008). Sedimentological record of tsunamis on shallow-shelf areas: The case of the 1969 AD and 1755 AD tsunamis on the Portuguese Shelf off Lisbon. *Marine Geology*, 249(3–4), 283–293. <https://doi.org/10.1016/j.margeo.2007.12.004>
- Ammann, B., & Lotter, A. F. (1989). Late-glacial radiocarbon and palynostratigraphy on the Swiss Plateau. *Boreas*, 18(2), 109–126. <https://doi.org/10.1111/j.1502-3885.1989.tb00381.x>
- Apotsos, A., Gelfenbaum, G., & Jaffe, B. (2012). Time-dependent onshore tsunami response. *Coastal Engineering*, 64, 73–86. <https://doi.org/10.1016/j.coastaleng.2012.01.001>
- Apotsos, A., Gelfenbaum, G., Jaffe, B., Watt, S., Peck, B., Buckley, M., & Stevens, A. (2011). Tsunami inundation and sediment transport in a sediment-limited embayment on American Samoa. *Earth-Science Reviews*, 107(1–2), 1–11. <https://doi.org/10.1016/j.earscirev.2010.11.001>
- BAFU. (2009). Hydrologisches Jahrbuch der Schweiz 2008. *Umwelt-Wissen Nr. 0921* (p. 578). Swiss Federal Office for the Environment.
- Behrens, J., Løvholt, F., Jalayer, F., Lorito, S., Salgado-Gálvez, M. A., Sørensen, M., et al. (2021). Probabilistic tsunami hazard and risk analysis: A review of research gaps. *Frontiers of Earth Science*, 9, 114. <https://doi.org/10.3389/feart.2021.628772>
- Berger, M. J., George, D. L., LeVeque, R. J., & Mandli, K. T. (2011). The GeoClaw software for depth-averaged flows with adaptive refinement. *Advances in Water Resources*, 34(9), 1195–1206. <https://doi.org/10.1016/j.advwatres.2011.02.016>
- Billeter, J. (1923). Pfarrer Jakob Billeter von Aegeri und seine Chronik. *Heimat-Klänge, Sonntags-Beilage zu den «Zuger Nachrichten»*.
- Bobrowsky, P. T., & Marker, B. (Eds.). (2018). *Encyclopedia of Engineering Geology*. Springer. <https://doi.org/10.1007/978-3-319-73568-9>
- Boggs, S., Jr. (2014). *Principles of sedimentology and stratigraphy* (5th ed., p. 564). Pearson.
- Bork, H. R., & Piorek, H. P. (2000). Integrierte Konzepte zum Schutz und zur dauerhaft-naturverträglichen Entwicklung mitteleuropäischer Landschaften—Chancen und Risiken, dargestellt am Beispiel des Boden- und Gewässerschutzes. In K. H. Erdman & T. J. Mager (eds.) *Innovative Ansätze zum Schutz der Natur* (pp. 69–83). Springer. https://doi.org/10.1007/978-3-642-56972-2_5
- Bosnic, I., Costa, P. J., Dourado, F., La Selle, S., & Gelfenbaum, G. (2021). Onshore flow characteristics of the 1755 CE Lisbon tsunami: Linking forward and inverse numerical modeling. *Marine Geology*, 434, 106432. <https://doi.org/10.1016/j.margeo.2021.106432>
- Bossard, P., Gammeter, S., Lehmann, C., Schanz, F., Bachofen, R., Bürgi, H. R., et al. (2001). Limnological description of the lakes Zürich, Lucerne, and Cadagno. *Aquatic Sciences*, 63(3), 225–249. <https://doi.org/10.1007/PL00001353>
- Bryant, E. (2014). Tsunami dynamics. In *Tsunami* (pp. 19–32). Springer. https://doi.org/10.1007/978-3-319-06133-7_2
- Buffington, J. M., & Montgomery, D. R. (1997). A systematic analysis of eight decades of incipient motion studies, with special reference to gravel-bedded rivers. *Water Resources Research*, 33(8), 1993–2029. <https://doi.org/10.1029/96WR03190>
- Bünti, J. L. (1973). Chronik des Johann Laurentz Bünti, Landammann, 1661–1736. *Beiträge zur Geschichte Nidwaldens*, 34, 26–27.
- Camenisch, C. (2019). The potential of late medieval and early modern narrative sources from the area of modern Switzerland for the climate history of the fourteenth century. In *The crisis of the 14th century* (pp. 43–61). De Gruyter. <https://doi.org/10.1515/9783110660784-003>
- Choi, S. U., & Kwak, S. (2001). Theoretical and probabilistic analyses of incipient motion of sediment particles. *KSCE Journal of Civil Engineering*, 5(1), 59–65. <https://doi.org/10.1007/BF02830727>
- Costa, P. J. M., & Andrade, C. (2020). Tsunami deposits: Present knowledge and future challenges. *Sedimentology*, 67(3), 1189–1206. <https://doi.org/10.1111/sed.12724>
- Costa, P. J. M., Feist, L., Dawson, A. G., Stewart, I., Reichert, K., & Andrade, C. (2021). An overview on offshore tsunami deposits. In T. Shiki, T. Yamazaki, Y. Tsuji, & F. Nanayama (eds.) *Tsunamiites*, (2nd ed., pp. 183–192). Elsevier. <https://doi.org/10.1016/B978-0-12-823939-1.00011-2>
- Cysat, R. (1969). Collectanea Chronica und denkwürdige Sachen pro Chronica Lucernensi et Helvetiae. In J. Schmid, & D. Schilling (Eds.), *Erster Band, zweiter Teil* (pp. 879–888). Diebold Schilling Verlag.
- Davies, H. L., Davies, J. M., Perembo, R. C. B., & Lus, W. Y. (2003). The Aitape 1998 tsunami: Reconstructing the event from interviews and field mapping. *Pure and Applied Geophysics*, 160, 1895–1922. <https://doi.org/10.1007/s00024-003-2413-1>
- Dawson, A. G., & Stewart, I. (2008). Offshore tractive current deposition: The forgotten tsunami sedimentation process. In T. Shiki, T. Yamazaki, Y. Tsuji, & A. Minoura (eds.) *Tsunamiites* (1st ed., pp. 153–161). Elsevier. <https://doi.org/10.1016/B978-0-444-51552-0.00010-2>

Acknowledgments

This study was funded by the Swiss National Science Foundation (research grant no. 171017) and is embedded in the SNSF Sinergia Project “Lake tsunami: causes, controls and hazard.” The authors thank Pedro Costa, Raphaël Paris, and an anonymous reviewer and the associate editor Alina Polonia for their constructive and informative reviews. The authors acknowledge Nicole Schwendener and the Institute of Forensic Medicine, University of Bern for their support with CT scanning. We thank Daniela Fischer and the Institute of Geography, University of Bern for their support with the grain-size determination. Sönke Szidat and the Department of Chemistry and Biochemistry, University of Bern are acknowledged for the radiocarbon dating. Julijana Krbanjevic is acknowledged for her help with the geochemical analysis. Fritz Schlunegger, Andy Lotter, and Beat Keller are thanked for their useful comments on the manuscript. Timothy Schmid is thanked for his fantastic help with Matlab codes. I am very grateful to Franzyska Nyffenegger, Dominik Amschwand, Julijana Krbanjevic, Flavio Huber, Evelyne Margelisch, Michael Strupler, Stefano Fabbri, Adrian Gilli, and Marina Morlock for their support during the coring campaign. Nikola Janevski is thanked for his help in collecting lake-bed samples from a sailboat.

- Dietrich, J. (1689). *Diarium von P. Josef Dietrich von Einsiedeln (1645–1704)*. Bd. 6. Klosterarchiv Einsiedeln, KAE A.HB.6.
- Einsele, G., Chough, S. K., & Shiki, T. (1996). Depositional events and their records—an introduction. *Sedimentary Geology*, *104*(1–4), 1–9. [https://doi.org/10.1016/0037-0738\(95\)00117-4](https://doi.org/10.1016/0037-0738(95)00117-4)
- Fäh, D., Giardini, D., Kästli, P., Deichmann, N., Gisler, M., Schwarz-Zanetti, G., et al. (2011). ECOS-09 earthquake catalogue of Switzerland release 2011 report and database. Public catalogue, 17.4.2011 (Report SED/RISK/R/001/20110417). Swiss Seismological Service ETH Zürich.
- Fäh, D., Gisler, M., Jaggi, B., Kästli, P., Lutz, T., Masciadri, V., et al. (2009). The 1356 Basel earthquake: An interdisciplinary revision. *Geophysical Journal International*, *178*(1), 351–374. <https://doi.org/10.1111/j.1365-246X.2009.04130.x>
- Favrod, J. (1991). *La Chronique de Marius d'Avenches (455-581): Texte, Traduction et Commentaire*. Section d'histoire, Faculté des lettres, Université de Lausanne.
- Feldens, P., Schwarzer, K., Szczucinski, W., Stattegger, K., Sakuna, D., & Sompongchaiyuk, P. (2009). Impact of 2004 tsunami on seafloor morphology and offshore sediments, Pakarang Cape, Thailand. *Polish Journal of Environmental Studies*, *18*(1).
- Fritz, H. M., Kalligeris, N., Borrero, J. C., Broncano, P., & Ortega, E. (2008). The 15 August 2007 Peru tsunami runup observations and modeling. *Geophysical Research Letters*, *35*(10). <https://doi.org/10.1029/2008GL033494>
- Fujiwara, O. (2008). Bedforms and sedimentary structures characterizing tsunami deposits. In *Tsunamiites* (pp. 51–62). Elsevier. <https://doi.org/10.1016/B978-0-444-51552-0.00004-7>
- Funk, H., Buxtorf, A., Christ, P., Egli, D., Estoppey, D., Gebel, C., et al. (2013). Geologischer Atlas der Schweiz, Blatt 1170, Alpnach (Nr. 137). Schweizerische Geologische Kommission.
- Gardner, J. V., Mayer, L. A., & Hughs Clarke, J. E. (2000). Morphology and processes in Lake Tahoe (California-Nevada). *The Geological Society of America Bulletin*, *112*(5), 736–746. [https://doi.org/10.1130/0016-7606\(2000\)112<736:MAPILT>2.0.CO;2](https://doi.org/10.1130/0016-7606(2000)112<736:MAPILT>2.0.CO;2)
- Gilli, A., Anselmetti, F. S., Glur, L., & Wirth, S. B. (2013). Lake sediments as archives of recurrence rates and intensities of past flood events. In M. Schneuwyl-Bollschweiler, M. Stoffel, & F. Rudolf-Miklau (eds.), *Dating Torrential Processes on Fans and Cones. Advances in Global Change Research* (Vol. 47). Springer. https://doi.org/10.1007/978-94-007-4336-6_15
- Glaser, R. (2008). *Klimageschichte Mitteleuropas, 1200 Jahre Wetter, Klima, Katastrophen: Mit Prognosen für das 21. Jahrhundert*. Wissenschaftliche Buchgesellschaft.
- Goodman-Tchernov, B. N., & Austin, J. A., Jr. (2015). Deterioration of Israel's Caesarea Maritima's ancient harbor linked to repeated tsunami events identified in geophysical mapping of offshore stratigraphy. *Journal of Archaeological Science: Report*, *3*, 444–454. <https://doi.org/10.1016/j.jasrep.2015.06.032>
- Goodman-Tchernov, B. N., Dey, H. W., Reinhardt, E. G., McCoy, F., & Mart, Y. (2009). Tsunami waves generated by the Santorini eruption reached Eastern Mediterranean shores. *Geology*, *37*(10), 943–946. <https://doi.org/10.1130/G25704A.1>
- Goto, K., Chagué-Goff, C., Fujino, S., Goff, J., Jaffe, B., Nishimura, Y., et al. (2011). New insights of tsunami hazard from the 2011 Tohoku-oki event. *Marine Geology*, *290*(1–4), 46–50. <https://doi.org/10.1016/j.margeo.2011.10.004>
- Goto, K., Ikehara, K., Goff, J., Chagué-Goff, C., & Jaffe, B. (2014). The 2011 Tohoku-oki tsunami—three years on. *Marine Geology*, *358*, 2–11. <https://doi.org/10.1016/j.margeo.2014.08.008>
- Goto, K., Takahashi, J., Oie, T., & Imamura, F. (2011). Remarkable bathymetric change in the nearshore zone by the 2004 Indian Ocean tsunami: Kirinda Harbor, Sri Lanka. *Geomorphology*, *127*(1–2), 107–116. <https://doi.org/10.1016/j.geomorph.2010.12.011>
- Grilli, S. T., Tappin, D. R., Carey, S., Watt, S. F., Ward, S. N., Grilli, A. R., et al. (2019). Modelling of the tsunami from the December 22, 2018 lateral collapse of Anak Krakatau volcano in the Sunda Straits, Indonesia. *Scientific Reports*, *9*(1), 1–13. <https://doi.org/10.1038/s41598-019-48327-6>
- Hantke, R., Bollinger, D., & Kopp, J. (2005). Geologischer Atlas der Schweiz, Blatt 1151, Rigi (Nr. 116). Schweizerische Geologische Kommission.
- Haraguchi, T., Goto, K., Sato, M., Yoshinaga, Y., Yamaguchi, N., & Takahashi, T. (2013). Large bedform generated by the 2011 Tohoku-oki tsunami at Kesenuma Bay, Japan. *Marine Geology*, *335*, 200–205. <https://doi.org/10.1016/j.margeo.2012.11.005>
- Harbitz, C. B., Løvholt, F., Pedersen, G., & Masson, D. G. (2006). Mechanisms of tsunami generation by submarine landslides: A short review. *Norwegian Journal of Geology/Norsk Geologisk Forening*, *86*(3).
- Heidarzadeh, M., Muhari, A., & Wijanarto, A. B. (2019). Insights on the source of the 28 September 2018 Sulawesi tsunami, Indonesia based on spectral analyses and numerical simulations. *Pure and Applied Geophysics*, *176*(1), 25–43. <https://doi.org/10.1007/s00024-018-2065-9>
- Hilbe, M., & Anselmetti, F. S. (2014). Signatures of slope failures and river-delta collapses in a perialpine lake (Lake Lucerne, Switzerland). *Sedimentology*, *61*(7), 1883–1907. <https://doi.org/10.1111/sed.12120>
- Hilbe, M., & Anselmetti, F. S. (2015). Mass movement-induced tsunami hazard on perialpine Lake Lucerne (Switzerland): Scenarios and numerical experiments. *Pure and Applied Geophysics*, *172*(2), 545–568. <https://doi.org/10.1007/s00024-014-0907-7>
- Hilbe, M., Anselmetti, F. S., Eilertsen, R. S., Hansen, L., & Wildi, W. (2011). Subaqueous morphology of Lake Lucerne (Central Switzerland): Implications for mass movements and glacial history. *Swiss Journal of Geosciences*, *104*, 425–433. <https://doi.org/10.1007/s00015-011-0083-z>
- Houwing, E. J., & Van Rijn, L. C. (1998). In situ erosion Flume (ISEF): Determination of bed-shear stress and erosion of a kaolin bed. *Journal of Sea Research*, *39*(3–4), 243–253. [https://doi.org/10.1016/S1385-1101\(98\)00007-0](https://doi.org/10.1016/S1385-1101(98)00007-0)
- Houwman, K. T., & Van Rijn, L. C. (1999). Flow resistance in the coastal zone. *Coastal Engineering*, *38*(4), 261–273. [https://doi.org/10.1016/S0378-3839\(99\)00049-6](https://doi.org/10.1016/S0378-3839(99)00049-6)
- Hunt, J. E., Wynn, R. B., Masson, D. G., Talling, P. J., & Teagle, D. A. (2011). Sedimentological and geochemical evidence for multistage failure of volcanic island landslides: A case study from Icod landslide on north Tenerife, Canary Islands. *Geochemistry, Geophysics, Geosystems*, *12*(12). <https://doi.org/10.1029/2011GC003740>
- Huntington, K., Bourgeois, J., Gelfenbaum, G., Lynett, P., Jaffe, B., Yeh, H., & Weiss, R. (2007). Sandy signs of a tsunami's onshore depth and speed. *Eos, Transactions American Geophysical Union*, *88*(52), 577–578. <https://doi.org/10.1029/2007EO520001>
- Ikehara, K., Irino, T., Usami, K., Jenkins, R., Omura, A., & Ashi, J. (2014). Possible submarine tsunami deposits on the outer shelf of Sendai Bay, Japan resulting from the 2011 earthquake and tsunami off the Pacific coast of Tohoku. *Marine Geology*, *358*, 120–127. <https://doi.org/10.1016/j.margeo.2014.11.004>
- Ishizawa, T., Goto, K., Yokoyama, Y., & Goff, J. (2020). Dating tsunami deposits: Present knowledge and challenges. *Earth-Science Reviews*, *200*, 102971. <https://doi.org/10.1016/j.earscirev.2019.102971>
- Ismail-Meyer, K., Stolt, M. H., & Lindbo, D. L. (2018). Soil organic matter. In *Interpretation of micromorphological features of soils and regoliths* (pp. 471–512). Elsevier. <https://doi.org/10.1016/B978-0-444-63522-8.00017-6>
- Ivy-Ochs, S., Schäfer, J., Kubik, P. W., Synal, H. A., & Schlüchter, C. (2004). Timing of deglaciation on the northern Alpine Foreland (Switzerland). *Eclogae Geologicae Helveticae*, *97*, 47–55. <https://doi.org/10.1007/s00015-004-1110-0>
- Jaffe, B. E., Buckley, M., Richmond, B., Strotz, L., Etienne, S., Clark, K., et al. (2011). Flow speed estimated by inverse modeling of sandy sediment deposited by the 29 September 2009 tsunami near Satitua, east Upolu, Samoa. *Earth-Science Reviews*, *107*(1–2), 23–37. <https://doi.org/10.1016/j.earscirev.2011.03.009>

- Jaffe, B. E., & Gelfenbaum, G. (2007). A simple model for calculating tsunami flow speed from tsunami deposits. *Sedimentary Geology*, 200(3–4), 347–361. <https://doi.org/10.1016/j.sedgeo.2007.01.013>
- Jaffe, B. E., Goto, K., Sugawara, D., Richmond, B. M., Fujino, S., & Nishimura, Y. (2012). Flow speed estimated by inverse modeling of sandy tsunami deposits: Results from the 11 March 2011 tsunami on the coastal plain near the Sendai Airport, Honshu, Japan. *Sedimentary Geology*, 282, 90–109. <https://doi.org/10.1016/j.sedgeo.2012.09.002>
- Johnson, J. P., Delbecq, K., & Kim, W. (2017). Predicting paleohydraulics from storm surge and tsunami deposits: Using experiments to improve inverse model accuracy. *Journal of Geophysical Research: Earth Surface*, 122(4), 760–781. <https://doi.org/10.1002/2015JF003816>
- Keller, B. (2013). Geologische Geschichte der Luzerner Reuss. In G. Paravicini (ed.) *Gestautes Wasser – Regulierter See: Geschichte, Bau und Betrieb der Reusswehranlage in Luzern* (pp. 105–123). Kanton Luzern, Bau-, Umwelt- und Wirtschaftsdepartement, Dienststelle Verkehr und Infrastruktur (vif), Abteilung Naturgefahren.
- Keller, B. (2017). Massive rock slope failure in Central Switzerland: History, geologic–geomorphological predisposition, types and triggers, and resulting risks. *Landslides*, 14, 1633–1653. <https://doi.org/10.1007/s10346-017-0803-1>
- Keller, B. (2021). Lake Lucerne and its spectacular landscape. In *Landscapes and landforms of Switzerland* (pp. 305–323). Springer. https://doi.org/10.1007/978-3-030-43203-4_21
- Kempf, P., Moernaut, J., Van Daele, M., Vermassen, F., Vandoorne, W., Pino, M., et al. (2015). The sedimentary record of the 1960 tsunami in two coastal lakes on Isla de Chiloe, south central Chile. *Sedimentary Geology*, 328, 73–86. <https://doi.org/10.1016/j.sedgeo.2015.08.004>
- Kihara, N., Fujii, N., & Matsuyama, M. (2012). Three-dimensional sediment transport processes on tsunami-induced topography changes in a harbor. *Earth Planets and Space*, 64(10), 787–797. <https://doi.org/10.5047/eps.2011.05.036>
- Kiss, A. (2009). Floods and weather in 1342 and 1343 in the Carpathian basin. *Journal of Environmental Geography*, 2(3–4), 37–47.
- Klyuchevskii, A. V., Demyanovich, V. M., & Klyuchevskaya, A. A. (2012). The possibility of a tsunami on Lake Baikal. *Doklay Earth Sciences*, 442, 130–134. <https://doi.org/10.1134/S1028334X1201014X>
- Kopp, J., Bendel, L., & Buxtorf, A. (1955). Geologischer Atlas der Schweiz, Blatt 1150, Luzern (Nr. 28). *Schweizerische Geologische Kommission*.
- Kraft, J. C. (1971). Sedimentary facies patterns and geologic history of a Holocene marine transgression. *The Geological Society of America Bulletin*, 82(8), 2131–2158. [https://doi.org/10.1130/0016-7606\(1971\)82\[2131:SFPAGH\]2.0.CO;2](https://doi.org/10.1130/0016-7606(1971)82[2131:SFPAGH]2.0.CO;2)
- Kremer, K., Anselmetti, F. S., Evers, F. M., Goff, J., & Nigg, V. (2021). Freshwater (paleo) tsunamis – A review. *Earth-Science Reviews*, 212(103447). <https://doi.org/10.1016/j.earscirev.2020.103447>
- Kremer, K., Hilbe, M., Simpson, G., Decrouy, L., Wildi, W., & Girardclos, S. (2015). Reconstructing 4000 years of mass movement and tsunami history in a deep peri-Alpine lake (Lake Geneva, France-Switzerland). *Sedimentology*, 62(5), 1305–1327. <https://doi.org/10.1111/sed.12190>
- Kremer, K., Simpson, G., & Girardclos, S. (2012). Giant Lake Geneva tsunami in ad 563. *Nature Geoscience*, 5(11), 756–757. <https://doi.org/10.1038/ngeo1618>
- Kuenen, P. H. (1953). Significant features of graded bedding. *AAPG Bulletin*, 37(5), 1044–1066. <https://doi.org/10.1306/SCEADCC8-16BB-11D7-8645000102C1865D>
- Kuenen, P. H., & Menard, H. W. (1952). Turbidity currents, graded and non-graded deposits. *Journal of Sedimentary Research*, 22(2), 83–96. <https://doi.org/10.1306/D42694CC-2B26-11D7-8648000102C1865D>
- Kuriyama, Y., Chida, Y., Uno, Y., & Honda, K. (2020). Numerical simulation of sedimentation and erosion caused by the 2011 Tohoku tsunami in Oarai Port, Japan. *Marine Geology*, 427, 106225. <https://doi.org/10.1016/j.margeo.2020.106225>
- Lampela, K. M. (2019). Tsunami shoaling theory. *Computational Methods and Experimental Measurements XIX & Earthquake Resistant Engineering Structures XII*. <https://doi.org/10.2495/ERES190101>
- Lee, H., & Balachandar, S. (2012). Critical shear stress for incipient motion of a particle on a rough bed. *Journal of Geophysical Research*, 117(F1). <https://doi.org/10.1029/2011JF002208>
- Løvholt, F., Bondevik, S., Laberg, J. S., Kim, J., & Boylan, N. (2017). Some giant submarine landslides do not produce large tsunamis. *Geophysical Research Letters*, 44(16), 8463–8472. <https://doi.org/10.1002/2017GL074062>
- Løvholt, F., Pedersen, G., Harbitz, C. B., Glimsdal, S., & Kim, J. (2015). On the characteristics of landslide tsunamis. *Philosophical Transactions of the Royal Society A: Mathematical, Physical & Engineering Sciences*, 373(2053), 20140376. <https://doi.org/10.1098/rsta.2014.0376>
- Mantz, P. A. (1977). Incipient transport of fine grains and flakes by fluids—extended shield diagram. *Journal of the Hydraulics Division*, 103(6), 601–615. <https://doi.org/10.1061/JYCEAJ.0004766>
- Michel, C., Bleicher, N., Brombacher, C., Hüster Plogmann, H., Ismail-Meyer, K., & Rehazek, A. (2012). Pfahlbauten am Vierwaldstättersee—der steinzeitliche Siedlungsplatz in Kehrsiten. *Archäologie der Schweiz*, 35(2), 56–71.
- Middleton, G. V. (1967). Experiments on density and turbidity currents: III. Deposition of sediment. *Canadian Journal of Earth Sciences*, 4(3), 475–505. <https://doi.org/10.1139/e67-025>
- Miller, D. J. (1961). Giant waves in Lituya Bay, Alaska. *U. S. Geological Survey, Professional Paper*, 354, 51–86. <https://doi.org/10.3133/pp354C6>
- Monecke, K., Anselmetti, F. S., Becker, A., Sturm, M., & Giardini, D. (2004). The record of historic earthquakes in lake sediments of Central Switzerland. *Tectonophysics*, 394(1–2), 21–40. <https://doi.org/10.1016/j.tecto.2004.07.053>
- Monecke, K., Finger, W., Klarer, D., Kongko, W., McAdoo, B. G., Moore, A. L., & Sudrajat, S. U. (2008). A 1,000-year sediment record of tsunami recurrence in northern Sumatra. *Nature*, 455(7217), 1232–1234. <https://doi.org/10.1038/nature07374>
- Montandon, F. (1925). Les Eboulements de la Dent du Midi et du Grammont (Examen critique de la Question du Tauredunum). *Le Globe. Revue genevoise de géographie*, 64(1), 35–91. <https://doi.org/10.3406/globe.1925.2349>
- Moore, J. G., Schweickert, R. A., Robinson, J. E., Lahren, M. M., & Kitts, C. A. (2006). Tsunami-generated boulder ridges in Lake Tahoe, California-Nevada. *Geology*, 34(11), 965–968. <https://doi.org/10.1130/G22643A.1>
- Mountjoy, J. J., Wang, X., Woelz, S., Fitzsimons, S., Howarth, J. D., Orpin, A. R., & Power, W. (2019). Tsunami hazard from lacustrine mass wasting in Lake Tekapo, New Zealand. *Geological Society, London, Special Publications*, 477(1), 413–426. <https://doi.org/10.1144/SP477.21>
- Mulder, T., Migeon, S., Savoye, B., & Jouanneau, J. M. (2001). Twentieth century floods recorded in the deep Mediterranean sediments. *Geology*, 29(11), 1011–1014. [https://doi.org/10.1130/0091-7613\(2001\)029<1011:TCFRIT>2.0.CO;2](https://doi.org/10.1130/0091-7613(2001)029<1011:TCFRIT>2.0.CO;2)
- Nanayama, F., Furukawa, R., Shigeno, K., Makino, A., Soeda, Y., & Igarashi, Y. (2007). Nine unusually large tsunami deposits from the past 4000 years at Kiritappu marsh along the southern Kuril Trench. *Sedimentary Geology*, 200(3–4), 275–294. <https://doi.org/10.1016/j.sedgeo.2007.01.008>
- Nigg, V., Bacigaluppi, P., Vetsch, D. F., Vogel, H., Kremer, K., & Anselmetti, F. S. (2021). Shallow-water tsunami deposits: Evidence from sediment cores and wave propagation of the 1601 CE Lake Lucerne Event. *PANGAEA*. <https://doi.org/10.1594/PANGAEA.938716>
- Nigg, V., Wohlwend, S., Hilbe, M., Bellwald, B., Fabbri, S. C., de Souza, G. F., et al. (2021). A tsunamigenic delta collapse and its associated tsunami deposits in and around Lake Sils, Switzerland. *Natural Hazards*, 1–35. <https://doi.org/10.1007/s11069-021-04533-y>

- Noda, A., Katayama, H., Sagayama, T., Suga, K., Uchida, Y., Satake, K., et al. (2007). Evaluation of tsunami impacts on shallow marine sediments: An example from the tsunami caused by the 2003 Tokachi-oki earthquake, northern Japan. *Sedimentary Geology*, 200(3–4), 314–327. <https://doi.org/10.1016/j.sedgeo.2007.01.010>
- Okal, E. A., & Synolakis, C. E. (2004). Source discriminants for near-field tsunamis. *Geophysical Journal International*, 158(3), 899–912. <https://doi.org/10.1111/j.1365-246X.2004.02347.x>
- Ontowirjo, B., Paris, R., & Mano, A. (2013). Modeling of coastal erosion and sediment deposition during the 2004 Indian Ocean tsunami in Lhok Nga, Sumatra, Indonesia. *Natural Hazards*, 65(3), 1967–1979. <https://doi.org/10.1007/s11069-012-0455-3>
- Palmer, A. P., Bendle, J. M., MacLeod, A., Rose, J., & Thorndycraft, V. R. (2019). The micromorphology of glaciolacustrine varve sediments and their use for reconstructing palaeoglaciological and palaeoenvironmental change. *Quaternary Science Reviews*, 226, 105964. <https://doi.org/10.1016/j.quascirev.2019.105964>
- Paris, A., Heinrich, P., Paris, R., & Abadie, S. (2020). The December 22, 2018 Anak Krakatau, Indonesia, landslide and tsunami: Preliminary modeling results. *Pure and Applied Geophysics*, 177(2), 571–590. <https://doi.org/10.1007/s00024-019-02394-y>
- Paris, R., Fournier, J., Poizat, E., Etienne, S., Morin, J., Lavigne, F., & Wassmer, P. (2010). Boulder and fine sediment transport and deposition by the 2004 tsunami in Lhok Nga (western Banda Aceh, Sumatra, Indonesia): A coupled offshore-onshore model. *Marine Geology*, 268(1–4), 43–54. <https://doi.org/10.1016/j.margeo.2009.10.011>
- Pfister, C., & Hächler, S. (1991). Überschwemmungskatastrophen im Schweizer Alpenraum seit dem Spätmittelalter. Raumzeitliche Rekonstruktion von Schadensmustern auf der Basis historischer Quellen. *Historische Klimatologie in verschiedenen Klimazonen* (Vol. 80, pp. 127–148). Selbstverlag des Instituts für Geographie der Universität Würzburg Würzburg.
- Pritchard, D., & Dickinson, L. (2008). Modelling the sedimentary signature of long waves on coasts: Implications for tsunami reconstruction. *Sedimentary Geology*, 206(1–4), 42–57. <https://doi.org/10.1016/j.sedgeo.2008.03.004>
- Putra, P. S., Aswan, A., Maryunani, K. A., Yulianto, E., Nugroho, S. H., & Setiawan, V. (2020). Post-event field survey of the 22 December 2018 Anak Krakatau tsunami. *Pure and Applied Geophysics*, 177, 2377–2429. <https://doi.org/10.1007/s00024-020-02446-8>
- Ramsey, C. B. (2009). Bayesian analysis of radiocarbon dates. *Radiocarbon*, 51(1), 337–360. <https://doi.org/10.1017/S0033822200033865>
- Reber, R., Akçar, N., Ivy-Ochs, S., Tikhomirov, D., Burkhalter, R., Zahno, C., et al. (2014). Timing of retreat of the Reuss Glacier (Switzerland) at the end of the Last Glacial Maximum. *Swiss Journal of Geosciences*, 107, 293–307. <https://doi.org/10.1007/s00015-014-0169-5>
- Reimer, P. J., Austin, W. E., Bard, E., Bayliss, A., Blackwell, P. G., Ramsey, C. B., et al. (2020). The IntCal20 northern hemisphere radiocarbon age calibration curve (0–55 cal kBP). *Radiocarbon*, 62(4), 725–757. <https://doi.org/10.1017/RDC.2020.41>
- Reimer, P. J., Brown, T. A., & Reimer, R. W. (2004). Discussion: Reporting and calibration of post-bomb ¹⁴C data. *Radiocarbon*, 46(3), 1299–1304. <https://doi.org/10.1017/S0033822200033154>
- Riou, B., Chaumillon, E., Schneider, J. L., Corrège, T., & Chagué, C. (2020). The sediment-fill of Pago Pago Bay (Tutuila Island, American Samoa): New insights on the sediment record of past tsunamis. *Sedimentology*, 67(3), 1577–1600. <https://doi.org/10.1111/sed.12574>
- Roberts, N. J., McKillop, R. J., Lawrence, M. S., Psutka, J. F., Clague, J. J., Brideau, M. A., & Ward, B. C. (2013). Impacts of the 2007 landslide-generated tsunami in Chehalis Lake, Canada. In *Landslide science and practice* (pp. 133–140). Springer. https://doi.org/10.1007/978-3-642-31319-6_19
- Röbke, B. R., & Vött, A. (2017). The tsunami phenomenon. *Progress in Oceanography*, 159, 296–322. <https://doi.org/10.1016/j.pocan.2017.09.003>
- Sakuna, D., Szczygiński, W., Feldens, P., Schwarzer, K., & Khokiatiwong, S. (2012). Sedimentary deposits left by the 2004 Indian Ocean tsunami on the inner continental shelf offshore of Khao Lak, Andaman Sea (Thailand). *Earth Planets and Space*, 64, 11. <https://doi.org/10.5047/eps.2011.08.010>
- Schaller-Donauer, A. (1937). *Chronik der Naturereignisse im Urnerland 1000–1800*. Gotthard Post.
- Schlunegger, F., Matter, A., Burbank, D. W., & Klaper, E. M. (1997). Magnetostratigraphic constraints on relationships between evolution of the central Swiss Molasse basin and Alpine orogenic events. *The Geological Society of America Bulletin*, 109(2), 225–241. [https://doi.org/10.1130/0016-7606\(1997\)109<0225:MCORBE>2.3.CO;2](https://doi.org/10.1130/0016-7606(1997)109<0225:MCORBE>2.3.CO;2)
- Schnellmann, M., Anselmetti, F. S., Giardini, D., & McKenzie, J. A. (2005). Mass movement-induced fold-and-thrust belt structures in unconsolidated sediments in Lake Lucerne (Switzerland). *Sedimentology*, 52(2), 271–289. <https://doi.org/10.1111/j.1365-3091.2004.00694.x>
- Schnellmann, M., Anselmetti, F. S., Giardini, D., & McKenzie, J. A. (2006). 15,000 Years of mass-movement history in Lake Lucerne: Implications for seismic and tsunami hazards. *Eclogae Geologicae Helveticae*, 99, 409–428. <https://doi.org/10.1007/s00015-006-1196-7>
- Schnellmann, M., Anselmetti, F. S., Giardini, D., McKenzie, J. A., & Ward, S. (2002). Prehistoric earthquake history revealed by lacustrine slump deposits. *Geology*, 30(12), 1131–1134. [https://doi.org/10.1130/0091-7613\(2002\)030<1131:PEHRBL>2.0.CO;2](https://doi.org/10.1130/0091-7613(2002)030<1131:PEHRBL>2.0.CO;2)
- Schwarz-Zanetti, G., Deichmann, N., Fäh, D., Giardini, D., Jimenez, M.-J., Masciadri, V., et al. (2003). The earthquake in Unterwalden on September 18, 1601: A historic-critical macroseismic evaluation. *Eclogae Geologicae Helveticae*, 96(3), 441–450.
- Shields, A. (1936). *Anwendung der Ähnlichkeitsmechanik und der Turbulenzforschung auf die Geschiebepbewegung* (PhD Thesis). Technical University Berlin.
- Siegenthaler, C., Finger, W., & Kelts & Wang, K. S. (1987). Earthquake and seiche deposits in Lake Lucerne, Switzerland. *Eclogae Geologicae Helveticae*, 80(1), 241–260.
- Siegenthaler, C., & Sturm, M. (1991). Die Häufigkeit von Ablagerungen extremer Reuss-Hochwasser. *Die Sedimentationsgeschichte im Urnersee seit dem Mittelalter*.
- Smedile, A., De Martini, P. M., Pantosti, D., Bellucci, L., Del Carlo, P., Gasperini, L., et al. (2011). Possible tsunami signatures from an integrated study in the Augusta Bay offshore (Eastern Sicily—Italy). *Marine Geology*, 281(1–4), 1–13. <https://doi.org/10.1016/j.margeo.2011.01.002>
- Smedile, A., Molisso, F., Chagué, C., Iorio, M., De Martini, P. M., Pinzi, S., et al. (2020). New coring study in Augusta Bay expands understanding of offshore tsunami deposits (Eastern Sicily, Italy). *Sedimentology*, 67(3), 1553–1576. <https://doi.org/10.1111/sed.12581>
- Spiske, M., Piepenbreier, J., Benavente, C., & Bahlburg, H. (2013). Preservation potential of tsunami deposits on arid siliciclastic coasts. *Earth-Science Reviews*, 126, 58–73. <https://doi.org/10.1016/j.earscirev.2013.07.009>
- Spiske, M., Weiss, R., Bahlburg, H., Roskosch, J., & Amijaya, H. (2010). The TsuSedMod inversion model applied to the deposits of the 2004 Sumatra and 2006 Java tsunami and implications for estimating flow parameters of palaeo-tsunami. *Sedimentary Geology*, 224(1–4), 29–37. <https://doi.org/10.1016/j.sedgeo.2009.12.005>
- Strupler, M., Anselmetti, F. S., Hilbe, M., Kremer, K., & Wiemer, S. (2020). A workflow for the rapid assessment of the landslide-tsunami hazard in peri-alpine lakes. *Geological Society, London, Special Publications*, 500(1), 81–95. <https://doi.org/10.1144/sp500-2019-166>
- Strupler, M., Bacigaluppi, P., Kremer, K., Vetsch, D., Anselmetti, F., Boes, R., & Wiemer, S. (2020). Abschätzung der Gefährdung durch Tsunamis in perialpinen Seen infolge Unterwasserhangrutschungen. *Wasser, Energie, Luft*, 112(1), 11–16.
- Strupler, M., Danciu, L., Hilbe, M., Kremer, K., Anselmetti, F. S., Strasser, M., & Wiemer, S. (2018). A subaqueous hazard map for earthquake-triggered landslides in Lake Zurich, Switzerland. *Natural Hazards*, 90(1), 51–78. <https://doi.org/10.1007/s11069-017-3032-y>

- Strupler, M., Hilbe, M., Kremer, K., Danciu, L., Anselmetti, F. S., Strasser, M., & Wiemer, S. (2018). Subaqueous landslide-triggered tsunami hazard for Lake Zurich, Switzerland. *Swiss Journal of Geosciences*, *111*, 353–371. <https://doi.org/10.1007/s00015-018-0308-5>
- Stuiver, M., & Polach, H. A. (1977). Discussion reporting of ^{14}C data. *Radiocarbon*, *19*(3), 355–363. <https://doi.org/10.1017/S0033822200003672>
- Sugawara, D., Minoura, K., Nemoto, N., Tsukawaki, S., Goto, K., & Imamura, F. (2009). Foraminiferal evidence of submarine sediment transport and deposition by backwash during the 2004 Indian Ocean tsunami. *Island Arc*, *18*(3), 513–525. <https://doi.org/10.1111/j.1440-1738.2009.00677.x>
- Suzuki, W., Aoi, S., Sekiguchi, H., & Kunugi, T. (2011). Rupture process of the 2011 Tohoku-Oki mega-thrust earthquake (M9.0) inverted from strong-motion data. *Geophysical Research Letters*, *38*(7). <https://doi.org/10.1029/2011GL049136>
- Synolakis, C. E., Bardet, J. P., Borrero, J. C., Davies, H. L., Okal, E. A., Silver, E. A., et al. (2002). The slump origin of the 1998 Papua New Guinea tsunami. *Proceedings of the Royal Society of London. Series A: Mathematical, Physical and Engineering Sciences*, *458*(2020), 763–789. <https://doi.org/10.1098/rspa.2001.0915>
- Tamura, T., Sawai, Y., Ikehara, K., Nakashima, R., Hara, J., & Kanai, Y. (2015). Shallow-marine deposits associated with the 2011 Tohoku-oki tsunami in Sendai Bay, Japan. *Journal of Quaternary Science*, *30*(4), 293–297. <https://doi.org/10.1002/jqs.2786>
- Tang, H., & Weiss, R. (2015). A model for tsunami flow inversion from deposits (TSUFLIND). *Marine Geology*, *370*, 55–62. <https://doi.org/10.1016/j.margeo.2015.10.011>
- Tappin, D. R., Matsumoto, T., Watts, P., Satake, K., McMurtry, G. M., Matsuyama, M., et al. (1999). Sediment slump likely caused 1998 Papua New Guinea tsunami. *Eos, Transactions American Geophysical Union*, *80*(30), 329–340. <https://doi.org/10.1029/99EO00241>
- Thevenon, F., Adatte, T., Poté, J., & Spangenberg, J. E. (2012). Recent human-induced trophic change in the large and deep perialpine Lake Lucerne (Switzerland) compared to historical geochemical variations. *Palaeogeography, Palaeoclimatology, Palaeoecology*, *363*, 37–47. <https://doi.org/10.1016/j.palaeo.2012.08.010>
- Urlaub, M., Talling, P. J., & Masson, D. G. (2013). Timing and frequency of large submarine landslides: Implications for understanding triggers and future geohazard. *Quaternary Science Reviews*, *72*, 63–82. <https://doi.org/10.1016/j.quascirev.2013.04.020>
- Van den Bergh, G. D., Boer, W., De Haas, H., Van Weering, T. C., & Van Wijhe, R. (2003). Shallow marine tsunami deposits in Teluk Banten (NW Java, Indonesia), generated by the 1883 Krakatau eruption. *Marine Geology*, *197*(1–4), 13–34. [https://doi.org/10.1016/S0025-3227\(03\)00088-4](https://doi.org/10.1016/S0025-3227(03)00088-4)
- Van Rijn, L. C. (2007). Unified view of sediment transport by currents and waves. I: Initiation of motion, bed roughness, and bed-load transport. *Journal of Hydraulic Engineering*, *133*(6), 649–667. [https://doi.org/10.1061/\(asce\)0733-9429\(2007\)133:6\(649\)](https://doi.org/10.1061/(asce)0733-9429(2007)133:6(649))
- Vanzo, D., Peter, S., Vonwiller, L., Buergler, M., Weberndorfer, M., Siviglia, A., et al. (2021). BASEMENT v3: A modular freeware for river process modelling over multiple computational backends. *Environmental Modelling & Software*, *143*, 105102. <https://doi.org/10.1016/j.envsoft.2021.105102>
- Vetsch, D. F., Siviglia, A., Bacigaluppi, P., Bürgler, M., Caponi, F., Conde, D., et al. (2020). System manuals of BASEMENT, Version 3.1. Laboratory of Hydraulics, Glaciology and Hydrology (VAW), ETH Zurich. Retrieved from www.basement.ethz.ch
- Watts, P. (1998). Wavemaker curves for tsunamis generated by underwater landslides. *Journal of Waterway, Port, Coastal, and Ocean Engineering*, *124*(3), 127–137. [https://doi.org/10.1061/\(ASCE\)0733-950X\(1998\)124:3\(127\)](https://doi.org/10.1061/(ASCE)0733-950X(1998)124:3(127))
- Weiss, R., & Bahlburg, H. (2006). A note on the preservation of offshore tsunami deposits. *Journal of Sedimentary Research*, *76*(12), 1267–1273. <https://doi.org/10.2110/jsr.2006.110>
- Weiss, R., Fritz, H. M., & Wünnemann, K. (2009). Hybrid modeling of the mega-tsunami runup in Lituya Bay after half a century. *Geophysical Research Letters*, *36*(9). <https://doi.org/10.1029/2009GL037814>
- Wentworth, C. K. (1922). A scale of grade and class terms for clastic sediments. *The Journal of Geology*, *30*(5), 377–392. <https://doi.org/10.1086/622910>
- Wilhelm, B., Arnaud, F., Sabatier, P., Magand, O., Chapron, E., Courp, T., et al. (2013). Palaeoflood activity and climate change over the last 1400 years recorded by lake sediments in the north-west European Alps. *Journal of Quaternary Science*, *28*(2), 189–199. <https://doi.org/10.1002/jqs.2609>
- Wirth, S. B., Glur, L., Gilli, A., & Anselmetti, F. S. (2013). Holocene flood frequency across the Central Alps—solar forcing and evidence for variations in North Atlantic atmospheric circulation. *Quaternary Science Reviews*, *80*, 112–128. <https://doi.org/10.1016/j.quascirev.2013.09.002>
- Woodruff, J. D., Donnelly, J. P., Mohrig, D., & Geyer, W. R. (2008). Reconstructing relative flooding intensities responsible for hurricane-induced deposits from Laguna Playa Grande, Vieques, Puerto Rico. *Geology*, *36*(5), 391–394. <https://doi.org/10.1130/G24731A.1>
- Yoshikawa, S., Kanamatsu, T., Goto, K., Sakamoto, I., Yagi, M., Fujimaki, M., et al. (2015). Evidence for erosion and deposition by the 2011 Tohoku-oki tsunami on the nearshore shelf of Sendai Bay, Japan. *Geo-Marine Letters*, *35*(4), 315–328. <https://doi.org/10.1007/s00367-015-0409-3>